Atmospheric CO_2 dynamics in a coastal megacity: spatiotemporal patterns, sea–land breeze impacts, and anthropogenic–biogenic emission partitioning

Jinwen Zhang[1], Yongjian Liang[2], Chenglei Pei[2], Bo Huang[3], Yingyan Huang[2], Xiufeng Lian[1,3], Shaojie Song[4], Chunlei Cheng[1], Cheng Wu[1], Zhen Zhou[1], Junjie Li[5], Mei Li[1*]

[1]College of Environment and Climate, Institute of Mass Spectrometry and Atmospheric Environment, Guangdong Provincial Engineering Research Center for Online Source Apportionment System of Air Pollution, Guangdong–Hongkong–Macau Joint Laboratory of Collaborative Innovation for Environmental Quality, Jinan University, Guangzhou 511443, China

[2]Guangzhou Ecological and Environmental Monitoring Center Station, Guangdong, Guangzhou 510006, China

[3]Guangzhou Hexin Instrument Co., Ltd., Guangdong, Guangzhou 510530, China

[4]College of Environmental Science and Engineering, Nankai University, Tianjin 300350, China

[5]School of Environment, Beijing Jiaotong University, Beijing 100044, China

Correspondence to: Mei Li (limei@jnu.edu.cn)

Abstract. Attributing observed carbon dioxide (CO_2) to fossil-fuel emissions versus biogenic fluxes is essential for assessing urban mitigation, but in coastal megacities it is complicated by anthropogenic–biogenic coupling and sea–land breeze (SLB) circulation. Here we analyze Guangzhou using multi-site in situ CO_2 and CO measurements (January 2023–September 2024), transport footprints, and a site-specific $\Delta CO/\Delta CO_2$ (R_{CO}) relationship to resolve spatiotemporal variability, quantify SLB effects, and partition fossil-fuel (CO_2ff) and biogenic (CO_2bio) contributions without assimilating emission inventories. Along a coastal–urban–suburban gradient, the coastal site shows the largest seasonal amplitude (25.63 ppm), the vegetated site exhibits strong summertime diurnal amplitude (39.90 ppm), and the urban core is combustion-dominated; together, these gradients indicate a seasonally displaced coastal CO_2 "dome", whose maximum enhancement need not occur in the urban core. SLB effects are seasonal: SLB ventilates CO_2 in spring–winter but promotes summertime accumulation (+2.08 ppm) under stable stratification, accompanied by pronounced CO enhancements, consistent with trapped/recirculated combustion plumes. Regression-derived urban R_{CO} is consistent with reported post-2013 broad tightening of coal/industrial and vehicle-emission controls. Winter-afternoon urban CO_2ff attribution remains robust to transport-model configurations and quantified measurement/background uncertainty. Summer-afternoon CO_2bio is -3.59 ± 0.63 μmol m^{-2} s^{-1}, offsetting up to 60 % of concurrent CO_2ff. These results demonstrate that coastal dynamics and urban greening reshape observed CO_2 signals, highlighting that biogenic–anthropogenic decoupling and SLB-aware sampling are essential for the robust evaluation of carbon mitigation in coastal megacities.

1 Introduction

Atmospheric carbon dioxide (CO_2), the predominant anthropogenic driver of climate change, is accumulating at unprecedented rates in human history (WMO, 2024). Future CO_2 increments will exert stronger warming effects than equivalent past increases due to climate system feedbacks (He et al., 2023), making emission control imperative. Despite covering only 3 % of global land, urban areas generate over 70 % of carbon emissions (Crippa et al., 2021), positioning cities as critical arenas where mitigation policies, infrastructure transitions, and urban greening can drive measurable changes in urban carbon budgets (WMO, 2025).

Urban atmospheric CO_2 concentrations provide a complementary constraint to flux- or inventory-based assessments because they integrate surface emissions, biogenic exchange, and atmospheric transport over the upwind source area (Lin et al., 2003; Shusterman et al., 2018; Pitt et al., 2022). This integration, however, creates an attribution challenge because observed CO_2 variability reflects coupled effects of fossil-fuel emissions, biogenic fluxes, and meteorology/transport, and thus is not uniquely attributable to any single driver, although one factor may dominate in certain regimes, especially on diurnal to seasonal timescales (Xueref-Remy et al., 2018; Yang et al., 2021; Mitchell et al., 2018). The challenge is particularly acute in coastal megacities, where land–sea thermal contrasts and marine background inflow drive strong diurnal reversals in advection and boundary-layer structure (Leroyer et al., 2014; Lei et al., 2024). These dynamics complicate observational representativeness and source–sink separation, and can make inferred CO_2 enhancements sensitive to background selection under different transport regimes (Verhulst et al., 2017). Given their high exposure to climate-related hazards, especially flooding and storm impacts, coastal megacities are priority targets for climate-risk management, motivating robust, policy-relevant CO_2 emissions assessment (Kumar, 2021).

A range of approaches has been used to constrain urban carbon budgets, including bottom-up inventories, tower-based atmospheric observations, tracer/isotope measurements, and atmospheric inversions. Bottom-up inventories provide essential baselines, yet urban emissions remain uncertain and can differ across products because they depend on activity/emission-factor assumptions and proxy-based downscaling (Gately and Hutyra, 2017; Gurney et al., 2019). While radiocarbon (^{14}C) measurements provide robust fossil-fuel/biogenic partitioning (Turnbull et al., 2015; Berhanu et al., 2017; Wang et al., 2022), their high cost and discontinuous sampling limit their applicability for long-term, high-frequency monitoring. Similarly, eddy covariance (EC) measurements quantify net CO_2 fluxes within tower footprints (typically 1–2 km radius), yet the derived flux partitioning reflects only local-scale dynamics and cannot fully represent city-wide carbon exchange processes (Velasco et al., 2013; Menzer

and Mcfadden, 2017; Wu et al., 2022b). Fully three-dimensional (3-D) atmospheric inversions can assimilate concentration data to estimate city-scale emissions and quantify posterior uncertainty when observation networks adequately constrain boundary inflow and key transport uncertainties (Lauvaux et al., 2016; Lian et al., 2023). Yet in practice, urban inversions are often limited by incomplete observational coverage, representativeness (sub-grid) errors, and transport biases (Boon et al., 2016; Deng et al., 2017; Ye et al., 2020; Che et al., 2022b). They can also remain sensitive to choices of background/boundary conditions and prior assumptions, including those related to biogenic fluxes, which can be large and temporally variable during the growing season (Turnbull et al., 2018; Nalini et al., 2022; Ye et al., 2020). These constraints motivate complementary observation-driven frameworks that emphasize process-level interpretation of concentration variability while explicitly tracking uncertainty sources.

A defining coastal process is the sea–land breeze (SLB), a common mesoscale circulation driven by land–sea thermal contrast (Shen et al., 2021). In the Pearl River Estuary (PRE), SLB occurrence shows pronounced seasonality and spatial dependence, with spring-autumn maxima reported in parts of the region (You and Chi-Hung Fung, 2019; Mai et al., 2024b). SLB produces a clear diurnal reversal between onshore and offshore flow and can modify boundary-layer structure and mixing depth (Wu et al., 2013; Lei et al., 2024), complicating the interpretation of urban CO_2 variability. By contrast, inland basins/valleys lack marine inflow–outflow and may be shaped by lake–land breeze circulations (Yang et al., 2022) or other topography-modulated flows that can shift background conditions and the footprint representativeness of urban observations (Mitchell et al., 2018; Wang et al., 2021). Beyond the PRE, China's coastal basins exhibit distinct SLB seasonality (e.g., a summer maximum in the Bohai Rim, weak seasonality in the Yangtze River Delta, and an autumn maximum in the PRE) (Huang et al., 2025), likely driven by regional differences in large-scale wind fields and air–sea turbulent heat fluxes (Shen et al., 2024), and potentially modulated by coastline geometry and topographic constraints. Despite recognized impacts of SLB on air quality (Zhao et al., 2022; Wang et al., 2023; Zheng et al., 2024), only a few case studies have examined how SLB-driven recirculation of nocturnally respired CO_2 can perturb daytime coastal CO_2 measurements and may bias emission inversions (Ahmadov et al., 2007), and systematic quantification across coastal cities remains limited.

Urban greening reinforces the need for explicit source–sink separation because neglecting biogenic contributions can bias inferred urban emissions (Miller et al., 2020; Ye et al., 2020; Sargent et al., 2018). Moreover, urban vegetation is often highly fragmented and can be underrepresented in moderate-to-coarse remote-sensing land-cover/canopy products, which may miss fine-scale urban heterogeneity and thereby introduce additional

uncertainty (and potential bias) into satellite-driven biogenic flux estimates (Ma et al., 2022; Corro et al., 2025; Glauch et al., 2025). Green coverage within built-up urban areas is similarly high across major Chinese coastal megacities (e.g., Guangzhou: 43.7 % in 2023; Shenzhen: 44.0 % in 2023; Qingdao: 44.0 % in 2023; Tianjin: 38.2 % in 2023) (Guangzhou Municipal Bureau of Statistics, 2024; Shenzhen Municipal Bureau of Statistics, 2024; Qingdao Municipal Bureau of Statistics, 2024; Tianjin Municipal Bureau of Statistics, 2024), implying that biogenic exchange can be non-negligible when interpreting urban observations. For example, in coastal North American cities, high-resolution vegetation modeling in New York City indicates that summertime biogenic uptake can offset up to 40 % of afternoon anthropogenic CO_2 enhancements and can fully balance on-road traffic contributions (Wei et al., 2022), while a dense-sensor analysis in Los Angeles suggests that daytime biogenic exchange can consume up to 60 % of fossil-fuel emissions during the peak growing season (Kim et al., 2025). Recent advances, including emerging atmospheric constraints such as carbonyl sulfide (COS), further demonstrate the feasibility and value of more robust biogenic quantification in city carbon budgets (Soininen et al., 2025).

Taken together, three knowledge gaps limit the interpretation of coastal megacity CO_2 observations and their use for mitigation assessment: (i) how spatiotemporal CO_2 patterns vary across a coastal–urban–suburban gradient; (ii) how SLB-driven transport and boundary-layer mixing reshape diurnal and seasonal CO_2 signals through seasonally varying ventilation, boundary-layer depth, and atmospheric stability, which may differ from inland-city regimes; and (iii) how fossil-fuel and biogenic contributions can be robustly separated, with quantified uncertainty, in a coastal setting. To bridge these gaps, we investigate Guangzhou (Pearl River Delta, China) as a living laboratory: high GDP and population indicate strong energy and mobility demand and thus substantial fossil-fuel CO_2 emissions, while evergreen urban vegetation, a long growing season, and frequent SLB circulation can produce non-negligible biogenic signals and complex coastal transport. The policy context further elevates the value of attribution: Guangdong's emissions-trading system (ETS) has operated since 2013, alongside measures targeting energy structure, vehicle emissions, building efficiency, and urban greening.

Given this imperative to track changes in urban emissions and net carbon exchange, we use an observation-driven framework that complements atmospheric inversion approaches and interprets diurnal–seasonal variability by combining multi-site in-situ CO_2 and CO measurements with footprint-informed transport analysis (Lin et al., 2003; Fasoli et al., 2018). Unlike a formal Bayesian 3-D inversion, our framework targets process attribution of observed variability and quantifies robustness through sensitivity tests rather than posterior flux estimates. This approach emphasizes process-level interpretation of concentration variability while explicitly evaluating key uncertainty

sources. While CO is widely used to infer fossil-fuel CO_2, it carries inherent uncertainties due to varying emission ratios (R_{CO}), background variability, and atmospheric chemical processing (Turnbull et al., 2011; Chen et al., 2020; Griffin et al., 2007; Vimont et al., 2019). Footprint estimates are likewise sensitive to meteorological forcing and boundary-layer representation, and such transport sensitivities may be amplified under complex coastal mesoscale flows. We therefore quantify uncertainties associated with measurement and background selection, evaluate robustness to transport-model setup via STILT configuration tests, assess biospheric consistency using seasonal vegetation activity (e.g., NDVI), and utilize emission inventories for contextual comparison—using inter-inventory spread as a plausibility envelope for benchmarking rather than a validation target.

Accordingly, we aim to: (i) resolve spatiotemporal patterns of CO_2 across three sites spanning near-coastal (NS), urban-core (PY), and suburban (CH) environments; (ii) quantify how SLB modulates diurnal-seasonal CO_2 variability and interpret the contrasts in terms of changes in wind ventilation, boundary-layer depth, and seasonally varying atmospheric stability/stratification; and (iii) partition observed CO_2 enhancements at the urban site (PY) into fossil-fuel and biogenic components using CO and footprint information, with explicit uncertainty characterization via measurement/background terms and STILT configuration sensitivity tests.

2 Data and methodology

2.1 Observational sites

The high-precision greenhouse gas monitoring network in Guangzhou is illustrated in Fig. 1. Three stations—Nansha (NS), Panyu (PY), and Conghua (CH) are symmetrically distributed along the city's predominant south–north wind axis, representing coastal, urban, and suburban atmospheric conditions, respectively. Site selection criteria are detailed in the Supplement. All stations employ tower-based sampling at similar heights: NS and PY at 48 m, and CH at 40 m. Monitoring spanned from January 1, 2023, to September 30, 2024. From PY, the straight-line distances to NS and CH are 54 km and 89 km, respectively.

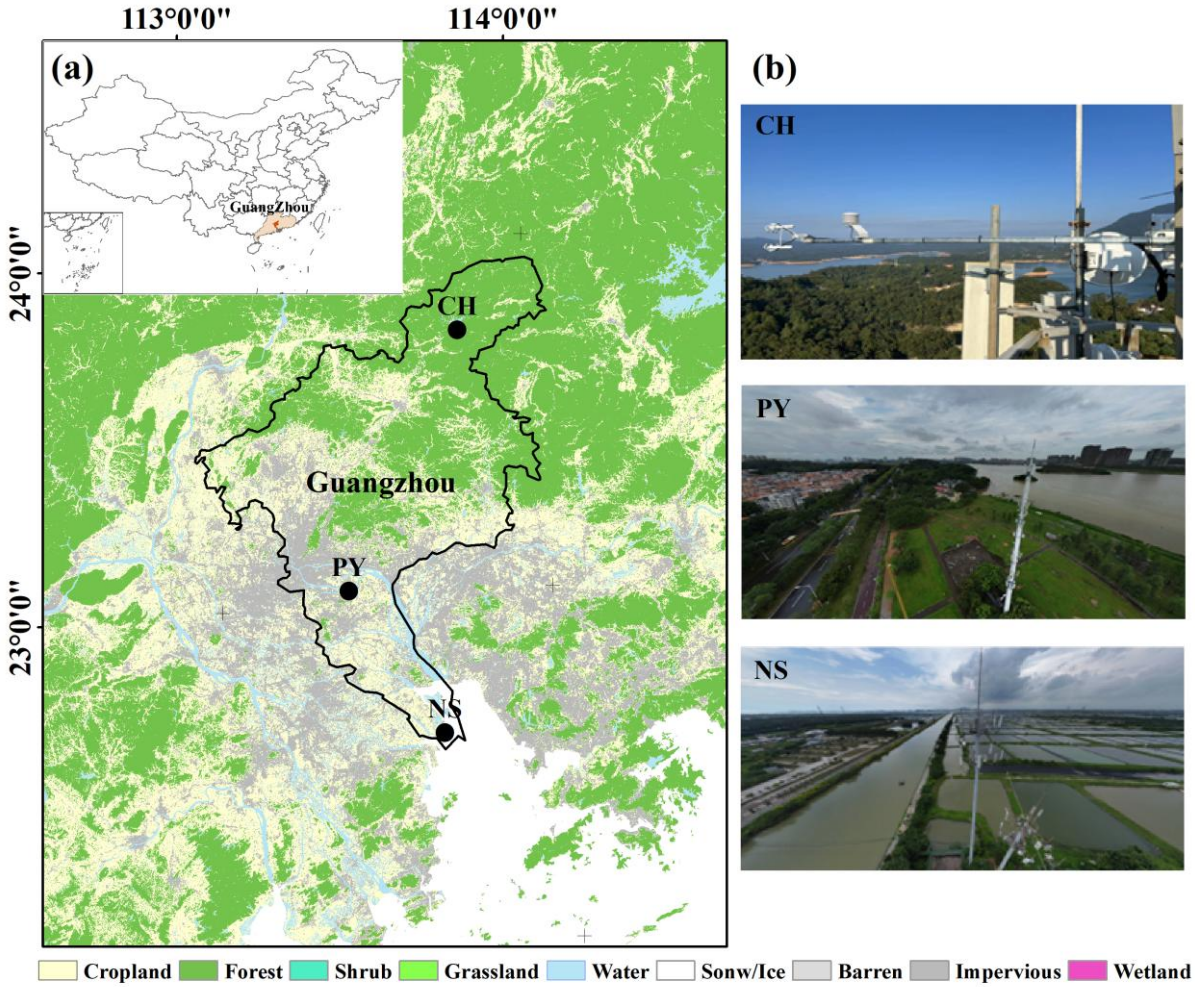

Figure 1. (a) Geographic locations of the NS, PY, and CH stations, with regional land use classification based on the 30 m resolution 2023 CLCD data (Yang and Huang, 2025). (b) Photograph of each station.

The NS station (113.63° E, 22.61° N) is located < 5 km from the coastline. This coastal site is surrounded by aquaculture ponds and sparse wetlands. Infrastructure nearby includes the under-construction southern extension of Guangzhou Metro Line 18 (NW direction) and the S78 highway (2 km west). The PY station (113.38° E, 23.03° N) is situated in the densely populated urban core; the tower is adjacent to Guangzhou University Town (north) and the Pearl River (south). A city road (100 m north) and the S73 expressway (700 m west) contribute to local emissions. The CH station (113.78° E, 23.74° N) is positioned in the northern suburbs. The site is bordered by subtropical evergreen broadleaf forests (north), a tourist resort (south), and a tea processing plant. The G45 highway lies 3 km northwest. According to the Emissions Database for Global Atmospheric Research (EDGAR) Community GHG database (EDGAR_2024_GHG; 2023; 0.1° × 0.1°) (Crippa et al., 2024), grid-level CO_2 emission densities for NS, PY, and CH are 3456, 15244, and 203 ton km^{-2} yr^{-1}, respectively (Fig. S1 in the Supplement).

2.2 Monitoring system

All three stations are equipped with similar monitoring systems, consisting of sampling modules, calibration

modules, gas analyzers, and data acquisition systems. Notably, the NS and PY stations utilize Picarro G2401 greenhouse gas analyzers to measure CO_2/CH_4/CO/H_2O, with a CO_2 measurement precision of < 20 ppb (5 min, 1 σ). The CH station employs an ABB GLA331-GGA greenhouse gas analyzer to measure CO_2/CH_4/H_2O, with a CO_2 measurement precision of < 25 ppb (5 min, 1 σ). N_2O and CO are measured using a GLA351-N2OCM analyzer. Detailed monitoring system and principles of the instruments are provided in the Supplement. Prior to field deployment, comparative tests were conducted in the laboratory to ensure the analytical performance consistency of the instruments. Additionally, meteorological sensors (measuring wind speed, direction, humidity, temperature, and pressure) are installed at the same height as the sampling inlets at NS and PY stations, while the CH station lacks such sensors. Detailed descriptions of wind field characteristics at NS and PY stations are included in the Supplement and illustrated in Fig. S2.

2.3 Calibration methods

The calibration module comprises two components: working standard curve establishment and target gas verification. High- and low-concentration standard gases are used to establish calibration curves, while a mid-concentration standard gas is used for target verification. The target and calibration gases are stored in inert-coated aluminum cylinders, uniformly supplied by the China National Environmental Monitoring Center. All stations follow the same calibration protocol: (1) weekly calibration curve establishment: high- and low-concentration gases are injected for 30 minutes each, with the final 5 minutes of instrument response used for calibration; (2) target gas verification every 12 h: mid-concentration gas is injected for 30 minutes, with the final 5 minutes of response used for verification; (3) re-calibration is triggered if the residual value (H) from target verification exceeds ± 0.2 ppm.

Calibration curves are derived from the instrument's response to calibration gas, yielding a linear calibration equation:

$$Y = A \times X - B, \quad (1)$$

where A, B are calibration coefficients. Calibrated CO_2 ($CO_{2,k}$) is calculated by:

$$CO_{2,k} = A \times CO_{2,m} - B, \quad (2)$$

where $CO_{2,m}$ is the measured response. Daily 12 h target gas verification is conducted to assess analyzer accuracy and stability by calculating the residual H:

$$H = \left(A \times CO_{2,c} - B\right) - CO_{2,n} \quad . \quad (3)$$

where $CO_{2,n}$ is the standard CO_2 concentration of the target gas, and $CO_{2,c}$ is the analyzer response/reading to the target gas.

To ensure high-precision and stable monitoring results, periods with |H| ⩽ 0.1 ppm are prioritized. Measurement uncertainties for the analyzers at NS, PY, and CH stations, calculated as the standard deviation (SD) of H (Yang et al., 2021), are 0.04, 0.02, and 0.04 ppm, respectively. In addition to daily calibration, maintenance personnel conduct weekly inspections of instruments and station facilities, including checks on power supply stability, data logger functionality, and industrial control computer status. Consumables (e.g., filters) are replaced as needed, and emergency repairs or instrument overhauls are performed when necessary. Any instrument downtime caused by internal or external factors is documented in maintenance logs, and affected data is flagged. Throughout the monitoring period, all three stations maintained data validity rates exceeding 90 %.

2.4 Sea–land breeze identification

The straight-line distances from the NS, PY, and CH stations to the coastline are 4, 58, and 130 km, respectively. The NS station, closest to the coast, was selected to study Guangzhou's sea–land breeze (SLB) circulation. Prior to SLB identification, local and background winds must be differentiated, as tower-measured winds (Fig. S2 in the Supplement) represent superimposed local and background wind fields, where strong background winds can obscure SLB signals (Qiu and Fan, 2013). The following equations distinguish background winds from local winds (Sun et al., 2022; Shen et al., 2019):

$$U_b = \overline{\sum_{i=0}^{23} U_i}\ , \tag{4}$$

$$V_b = \overline{\sum_{i=0}^{23} V_i}\ , \tag{5}$$

$$U_l = U_O - U_b\ , \tag{6}$$

$$V_l = V_O - V_b\ . \tag{7}$$

where U_O and V_O are the observed wind fields from the tower, U_b and V_b denote background winds, and U_l and V_l represent local winds.

A sea–land breeze day (SLBD) is defined as any 24 h period exhibiting a distinct transition from sea breezes during the day to land breezes at night (Xiao et al., 2023). SLB identification criteria vary regionally due to differences in topography and coastline geometry (Huang et al., 2025). Guided by the SLB criteria in Supplementary Table S1 and historical patterns for the Pearl River Estuary (Qiu and Fan, 2013; Zhang et al., 2024; Mai et al., 2024b), we define for the north-shore site (NS) directional sectors of 112–202° for the sea breeze and 302–45° for the land breeze. The corresponding detection windows are 12:00–20:00 LT (sea breeze) and 01:00–09:00 LT (land breeze),

consistent with regional SLB climatologies. Directional persistence is evaluated using the local-wind direction. The wind-speed screen is applied to the observed wind-speed magnitude at 48 m. A day is labeled as an SLB day only if all the following conditions are satisfied: (1) Directional persistence: within each window, the local wind direction (from the decomposed local component) stays inside the corresponding sector for ≥ 4 h, or for ≥ 4 h within any running 5 h window; and (2) Weak-forcing screen: for the same candidate SLB day, the observed wind-speed magnitude at 48 m must remain < 10 m s^{-1} at every hour of that day (i.e., no hourly value exceeds 10 m s^{-1}). This conservative cap follows coastal-China SLB climatologies and is intended to exclude strongly forced days (Qiu and Fan, 2013; Sun et al., 2022; Huang et al., 2025; Zhang et al., 2024). Otherwise, the day is designated a non-SLB day (NSLBD).

Together, these two requirements reduce the likelihood of misclassification under strongly forced conditions. Days dominated by synoptic forcing or tropical-cyclone peripheries often show a prolonged anomalous wind regime rather than a clear diurnal reversal (Atkins and Wakimoto, 1997; Allouche et al., 2023). To explicitly assess residual tropical-cyclone (TC) contamination, we cross-referenced the SLB calendar with 2023 Pearl River Delta (PRD)/Guangzhou TC impact windows compiled from the official Guangdong–Hong Kong–Macao Greater Bay Area (GBA) Climate Monitoring Bulletin (Table S2). For each TC, Impact Start/End are defined as the first/last local dates on which the bulletin reports PRD/Guangzhou impacts or advisories attributable to that system (including peripheral rainbands/gusts). Because the bulletin is date-based, we conservatively treat the entire day within each window as potentially TC-influenced. Only one SLBD (2 Sep 2023) falls within these windows; excluding it leaves results unchanged.

2.5 Estimation of CO_2tot, CO_2ff, and CO_2bio

The observed CO_2 concentration enhancements at tall-tower receptor sites represent the integrated influence of upwind surface fluxes transported by atmospheric advection and mixing (Lin et al., 2003). Consequently, upwind carbon emissions can be inferred from site-specific enhancement measurements coupled with their corresponding atmospheric footprints. Here we apply an observation-driven framework that combines concentration-enhancement observations with transport-model footprints to estimate total CO_2 (CO_2tot) and CO (COtot) surface fluxes, and to further derive fossil-fuel (CO_2ff) and biogenic (CO_2bio) components using the site-specific $\Delta CO/\Delta CO_2$ relationship (R_{CO}), without relying on any a priori emissions inventory. The required inputs are limited to enhancement observations at the receptor sites and atmospheric footprints, consistent with previous regional flux quantifications for CO_2, CH_4, and CO (Mitchell et al., 2018; Lin et al., 2021; Wu et al., 2022a). Emission inventories are used only

for site-context characterization (Sect. 2.1) and, subsequently, for an independent bottom-up plausibility envelope for winter-afternoon flux estimates (Sect. 3.5), rather than as priors or validation targets. CO_2tot and COtot are calculated as:

$$CO_2tot = \frac{CO_{2,s}obs - CO_2bg}{\sum_i Footprint_{i,s}}, \quad (8)$$

$$COtot = \frac{CO_s obs - CObg}{\sum_i Footprint_{i,s}}, \quad (9)$$

The numerators are hourly CO_2 and CO concentration enhancements (ΔCO_2 and ΔCO) at station s, where $CO_{2,s}$obs and CO_sobs represent observed CO_2 and CO concentrations, while CO_2bg and CObg denote urban background concentrations (detailed in the Supplement). The denominators are hourly total atmospheric footprints ($\sum_i \mathrm{Footprint}_{i,s}$), where i denotes backward particle release time from the receptor. Due to challenges in modeling mixed-layer depths during nighttime, morning, and evening, flux analysis focuses on afternoon hours (12:00–16:00) (Boon et al., 2016; Mitchell et al., 2018; Lin et al., 2021). Daily-scale CO_2tot and COtot are derived by dividing the mean afternoon ΔCO_2 and ΔCO by the corresponding mean $\sum_i \mathrm{Footprint}_{i,s}$. The footprint quantifies the sensitivity of concentration enhancements at the observation site to upwind surface fluxes, as detailed in Sect. 2.5.1. ΔCO_2 is in units of [ppm], while footprint is in [ppm / (μmol m^{-2} s^{-1})], so CO_2tot, the quotient between the two quantities, is in flux units of [μmol m^{-2} s^{-1}].

Anthropogenic CO_2 emissions (CO_2ff) are derived from COtot and the CO/CO_2 emission ratio (R_{CO}), where R_{CO} is determined from real-time tower-measured data, as described in detail in Sect. 3.4:

$$CO_2ff = \frac{COtot}{Rco}, \quad (10)$$

Biogenic fluxes (CO_2bio) are calculated as residuals:

$$CO_2bio = CO_2tot - CO_2ff. \quad (11)$$

Positive CO_2bio values indicate biogenic carbon emissions, while negative values denote carbon uptake, reflecting the dual role of urban biospheres as CO_2 sources and sinks (Kim et al., 2025).

2.5.1 Atmospheric transport model

To trace airmass sources entering the urban domain and reaching observation sites, and to assess CO_2 emissions corresponding to observed concentration enhancements, the Stochastic Time-Inverted Lagrangian Transport model (STILT-Rv2) was employed for atmospheric transport simulations, driven by meteorological fields from the Weather Research and Forecasting Model (WRFv4.1.1). In this study, STILT serves two purposes: (1) providing

airmass trajectories for identifying marine background concentrations in Guangzhou, and (2) generating atmospheric footprints for quantifying total CO_2 and CO emissions.

The STILT model simulates atmospheric transport by releasing a set of air particles backward in time from the receptor location at the observation height. These particles are tracked spatially and temporally as they disperse upwind. The resulting trajectories delineate source regions influencing the receptor site and quantify the sensitivity of observed concentrations to upwind surface fluxes, termed "source–receptor relationships" or "atmospheric footprints" (Lin et al., 2003; Fasoli et al., 2018). Footprints represent the contribution of upwind sources/sinks to downwind concentration changes, with higher sensitivities near receptors or under stable wind conditions, where boundary layer airmasses interact more directly with surface fluxes (Wu et al., 2022a). For this study, 500 particles were released at 48 m (PY station) heights, and traced backwards in time for 72 h. Footprints were computed at 0.08° × 0.08° spatial resolution. Periods with total footprint sensitivities ($\sum_i \mathrm{Footprint}_i$) below the 10th percentile were excluded, indicating low sensitivity to regional surface fluxes (Lin et al., 2021).

To evaluate whether STILT setup choices could bias the inferred fluxes, we performed targeted wintertime sensitivity experiments at PY using paired daily comparisons (n = 18). Starting from the baseline (500 particles, 0.08° grid, 72 h backward), we independently varied (1) particle number (1000, 2000), (2) grid resolution (0.05°, 0.10°), and (3) backward duration (96 h, 120 h). For each variant we recomputed footprints, reran the flux-estimation framework, and compared paired daily afternoon means (12:00–16:00 LT) of CO_2tot, CO_2ff and CO_2bio to the baseline using percent differences, Pearson r, and paired t-tests. Percent differences quantify effect size, Pearson r assesses day-to-day consistency, and paired t-tests evaluate detectability of systematic mean shifts. This paired-day design isolates transport-model parameter effects from day-to-day meteorology and observation sampling.

2.5.2 Uncertainty sources

Uncertainties associated with the emission estimates inferred from Eqs. (12)–(14) primarily arise from four sources: (1) observational uncertainty, (2) background concentration uncertainty, (3) atmospheric transport (footprint) uncertainty, and (4) R_{CO}-related uncertainty. We do not explicitly propagate transport/footprint uncertainty within the analytical error propagation of Eqs. (12)–(14); instead, we evaluate sensitivity to transport-model setup using a winter paired-day STILT sensitivity analysis (Sect. 2.5.1; Sect. 3.5; Fig. 11). Residual transport biases (e.g., winds and boundary-layer mixing) remain unquantified and may bias the inferred fluxes, thereby contributing to

inventory–observation differences when benchmarking against independent bottom-up inventories, alongside emission-inventory uncertainty and the representativeness mismatch between footprint-weighted enhancements and unweighted inventory means (discussed further in Sect. 3.5). Uncertainty associated with R_{CO} is not explicitly propagated as a formal regression-parameter uncertainty in this study; because R_{CO} is derived from CO and CO_2 enhancements, its uncertainty is expected to be driven mainly by uncertainties in the underlying enhancements (items 1–2) and scatter in the site-specific relationship. Among the quantified terms, uncertainties in CO_2tot are dominated by observational and background concentration errors. Uncertainties in CO_2ff are additionally affected by R_{CO}-related variability, while uncertainties in CO_2bio and the CO_2bio/CO_2ff offset ratio are propagated from CO_2tot and CO_2ff. Accordingly, the combined uncertainty term is calculated as:

$$E_u^2 = OBS_{u,c}^2 + BG_u^2 , \quad (12)$$

where $OBS_{u,c}$ represents uncertainty in urban atmospheric observations, and BG_u represents uncertainty in urban background concentrations. We cannot accurately quantify all error sources involved in instrumental measurements; some minor error sources (e.g., uncertainty related to water vapor) may be negligible, while the primary uncertainty originates from discrepancies between measured concentrations and calibration standards (Verhulst et al., 2017). Here, $OBS_{u,c}$ is calculated as the standard deviation (SD) of residuals H (Yang et al., 2021). For urban background uncertainties:

$$BG_{u,co2}^2 = CT_{co2,r}^2 + CT_{co2,s}^2 , \quad (13)$$

$$BG_{u,co}^2 = OBS_{co,r}^2 + OBS_{co,s}^2 . \quad (14)$$

CO_2 background uncertainty ($BG_{u,co2}$) combines the absolute monthly smoothed residuals ($CT_{co2,r}$) and variability (SD) of monthly CO_2 concentrations ($CT_{co2,s}$) from CarbonTracker (CT). Similarly, CO background uncertainty ($BG_{u,co}$) is derived from monthly smoothed residuals ($OBS_{co,r}$) and variability ($OBS_{co,s}$) of in situ observations.

To guard against bias from transport settings, the paired-day sensitivity analysis is conducted relative to the baseline; we treat effect sizes and 95 % confidence intervals (CIs) as primary quantities and report p-values only to indicate detectability given n = 18, with quantitative outcomes presented in Sect. 3.5 and Fig. 11.

3 Results and discussion

3.1 Spatiotemporal patterns of atmospheric CO_2

Figure 2 presents the hourly mean time series of atmospheric CO_2 concentrations at the NS, PY, and CH stations

in Guangzhou from January 1, 2023, to September 30, 2024. To assess wind field impacts on CO_2 variability (Fig. S2), concentrations were classified into five categories: local (wind speed < 1.5 m s^{-1}) and four directional sectors (wind speed ≥ 1.5 m s^{-1}) defined as NE (0–90°), SE (90–180°), SW (180–270°), and NW (270–360°). All stations exhibited significant temporal variability, with standard deviations (SD) of 13.90 (NS), 15.92 (PY), and 16.05 ppm (CH), consistent with urban and suburban observations in Hangzhou, Beijing, Xi'an, and Seoul (Park et al., 2021; Yang et al., 2021; Chen et al., 2024; Liu et al., 2025). PY showed the highest CO_2 levels and variability, driven predominantly by local-type emissions under low wind speeds. In contrast, the NS coastal station exhibited elevated concentrations during northerly winds (NW/NE). Seasonal wind effects were pronounced: summer southerly winds (SW/SE) generally reduced CO_2 at PY and NS (most notably at NS near the coast), while winter northerly winds (NW/NE) often increased CO_2 at NS.

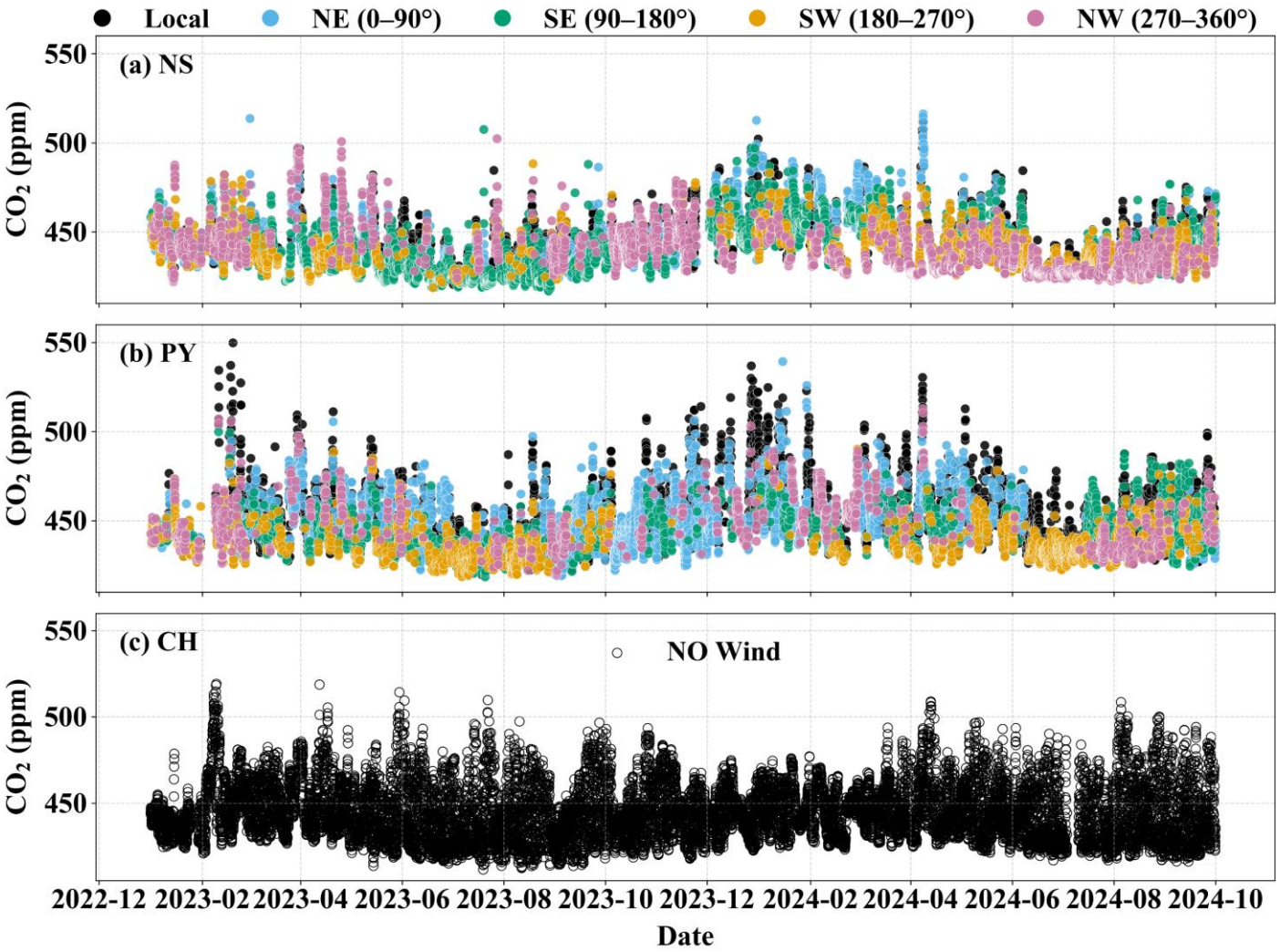

Figure 2. Time series of atmospheric CO_2 concentrations at the (a) NS, (b) PY, and (c) CH stations. For NS and PY, points are color-coded by wind category: local conditions (wind speed < 1.5 m s^{-1}) and four directional sectors for winds ≥ 1.5 m s^{-1} (NE, 0–90°; SE, 90–180°; SW, 180–270°; NW, 270–360°). For CH, wind-direction classification is not shown and the time series is plotted without sector coloring.

Urban–rural CO_2 gradients vary globally due to differences in economic activity, population density, land use, and energy infrastructure, reflecting heterogeneous urban carbon emissions (Gao et al., 2022). To further illustrate this spatial contrast and its seasonality, we summarized the urban–suburban/coastal gradients across the full record and report annual and seasonal means in Fig. 3. In Guangzhou, mean CO_2 concentration differences between PY and NS/CH were 6.67 and 3.43 ppm, respectively, forming a distinct "urban dome" (urban > suburban > coastal). The NS–CH difference (3.44 ppm) highlights comparable gradients between suburban and coastal zones. This gradient mirrors Los Angeles's coastal megacity profile but with a smaller magnitude (Verhulst et al., 2017). Guangzhou's urban–suburban difference (3.43 ppm) aligns with Hangzhou's 2021 observations (4.96 ppm) (Chen et al., 2024) but is lower than Nanjing (8.1 ppm, 2014) and Beijing (12.4 ppm, 2018–2019) (Gao et al., 2018; Yang et al., 2021). It remains far smaller than Shanghai (55.1 ppm, 2014) and Baltimore (66.0 ppm, 2002–2006) (Pan et al., 2016; George et al., 2007). Over time, urban emissions may stabilize as suburban populations and fossil fuel demand grow, potentially narrowing urban–suburban CO_2 differences (Mitchell et al., 2018). For instance, Hangzhou's reduced gradient reflects urbanization-driven energy consumption, where suburban monitoring captures urban emission influences (Chen et al., 2024).

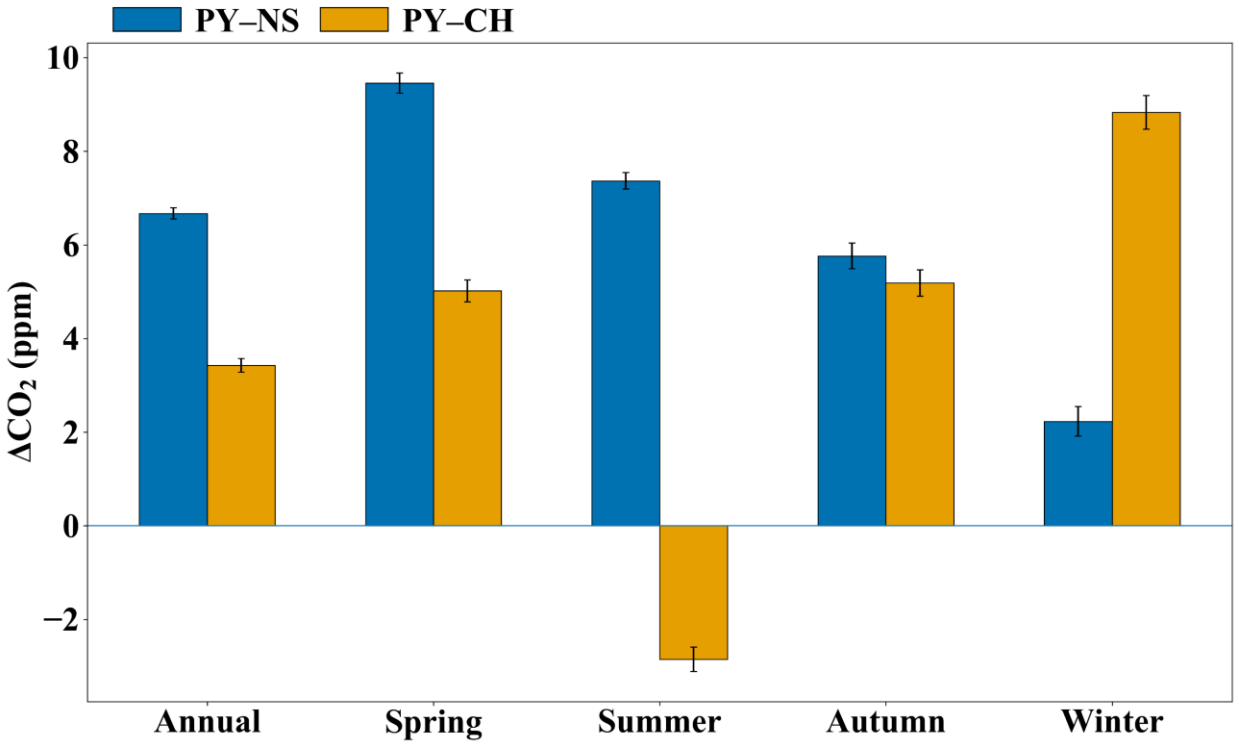

Figure 3. Urban–suburban/coastal CO_2 gradients in Guangzhou. Annual and seasonal mean concentration differences (ΔCO_2, ppm) between the urban site (PY) and the coastal site (NS) (PY–NS) and between PY and the suburban site (CH) (PY–CH). Seasons are defined as Spring (Mar–May), Summer (Jun–Aug), Autumn (Sep–Nov), and Winter (Dec–Feb). Error bars denote ± 1 standard error (SE).

Figure 3 further shows that these spatial gradients are strongly season-dependent. PY–NS remains positive year-

374 round but is smallest in winter (2.23 ppm), when prevailing northerlies elevate CO_2 at the coastal NS site and reduce
375 the urban–coastal contrast, consistent with Fig. 2. PY–CH is more strongly seasonally modulated: it peaks in winter
376 (8.83 ppm) but reverses sign in summer (−2.86 ppm), when southerly (marine-influenced) flow more frequently
377 ventilates PY (SW/SE sectors in Fig. 2) and the CH summertime enhancement may reflect a northward-displaced
378 urban influence plus biogenic/boundary-layer modulation (Sect. 3.1.1; Sect. 3.3). Spring and autumn show
379 intermediate positive PY–CH (~5 ppm), while PY–NS peaks in spring (9.46 ppm), consistent with enhanced coastal
380 ventilation under southerly influence. Together, these gradients indicate a seasonally displaced CO_2 "dome" in this
381 coastal setting, where the highest CO_2 within our network can occur outside the urban core, complementing the
382 site-level seasonal cycles discussed in Sect. 3.1.1. This coastal, seasonally displaced CO_2 dome contrasts with
383 patterns more commonly reported in inland megacity networks, where enhancements are typically strongest at the
384 most urbanized sites relative to suburban/background stations (Xueref-Remy et al., 2018; Yang et al., 2021; Chen
385 et al., 2024).

386 **3.1.1 Seasonal variability of atmospheric CO_2**

387 Figure 4 illustrates the monthly mean variations in atmospheric CO_2 concentrations at the NS, PY, and CH stations
388 in Guangzhou, alongside their correlations with the Normalized Difference Vegetation Index (NDVI). NDVI data
389 at 1 km × 1 km spatial resolution were obtained from NASA's EOSDIS Land Processes Distributed Active Archive
390 Center (Didan, 2015), with values within a 3 km radius buffer around each station center used for comparative
391 analysis. All three stations exhibited consistent seasonal CO_2 patterns, with higher concentrations in winter/spring
392 and lower values in summer/autumn, mirroring observations in Hangzhou (Chen et al., 2024). These variations
393 arise from the combined effects of (1) seasonal biogenic flux cycles, (2) anthropogenic emission variability, and (3)
394 boundary layer height dynamics (Xueref-Remy et al., 2018). Enhanced vegetation photosynthesis during warmer
395 months (summer/autumn, Table S3 in the Supplement) strengthens biogenic carbon sinks, while higher boundary
396 layer depths (Fig. S6 in the Supplement) and southerly marine air masses (Fig. 2) promote atmospheric mixing and
397 CO_2 dispersion.

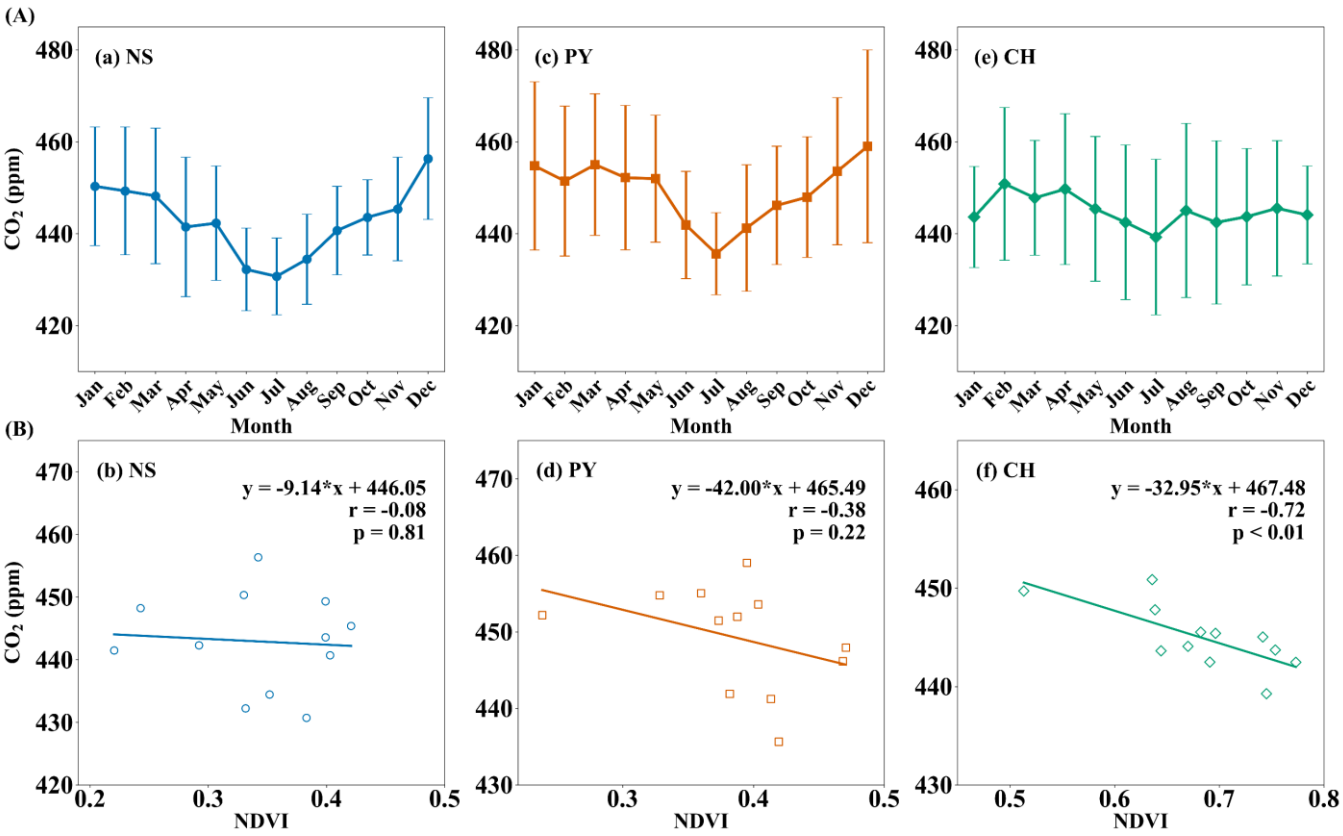

Figure 4. (A) Variations in monthly mean CO_2 concentrations and (B) their correlations with Normalized Difference Vegetation Index (NDVI) for the (a–b) NS, (c–d) PY, and (e–f) CH stations. Error bars indicate ± 1 standard deviation (SD).

The amplitudes of the seasonal variation of CO_2 at NS, PY, and CH are 25.63, 23.38, and 11.59 ppm, respectively. NS and PY peaked in December and troughed in July, whereas CH peaked in February and troughed in July. NS's large amplitude reflects its extreme December highs and July lows. In December, prevailing northerly winds (Figs. 2a and S2a) transported urban emissions to downwind NS, narrowing its CO_2 difference with PY to 2.68 ppm. Conversely, July saw NS's CO_2 concentrations fall to the lowest among all stations—4.93 ppm and 8.56 ppm below PY and CH, respectively—establishing a south-to-north increasing gradient (coastal < urban < suburban). This gradient aligns with marine-influenced southerly air masses, which dilute coastal CO_2 while transporting urban emissions northward, potentially accumulating CO_2 in northern suburbs. This south–north pattern is consistent with the seasonal mean gradients in Fig. 3, which summarize how the urban–coastal contrast weakens in winter and how the urban–suburban gradient can be seasonally displaced in summer.

Although CH exhibits strong biogenic coupling (NDVI–CO_2 correlation: −0.72; Fig. 4f), NS shows an opposite seasonal contrast relative to CH (−9.80 ppm in summer; +5.80 ppm in winter), pointing to transport- and boundary-layer-driven variability at the coastal site. At NS, the NDVI–CO_2 correlation is weak (−0.08) and NDVI varies within a narrow range (0.22–0.42), indicating limited local biogenic control, whereas seasonal shifts in marine–

continental transport (summer dilution vs. winter urban outflow) and boundary-layer depth jointly modulate dilution and accumulation (Figs. 2 and S6). In February, CH recorded its annual CO_2 maximum, driven by vegetation respiration during early growth stages and elevated emissions from fireworks around the Lunar New Year, as CH's location falls outside Guangzhou's fireworks restriction zones (https://www.gz.gov.cn/gfxwj/qjgfxwj/chq/qf/content/post_7198980.html, last access: 18 June 2025). This interpretation is supported by CO, a tracer for combustion-derived CO_2 (Newman et al., 2013; Che et al., 2022a): CH's CO concentrations also peaked in February due to firework emissions, whereas other sites peaked in December (Fig. S7 in the Supplement).

3.1.2 Diurnal variations of atmospheric CO_2

The diurnal patterns of atmospheric CO_2 concentrations at NS, PY, and CH stations in Guangzhou consistently exhibited lower daytime and higher nighttime values (Fig. 5). This is attributed to the shallow nocturnal boundary layer, which traps anthropogenic and biogenic fluxes near the surface, elevating CO_2 levels. After sunrise, surface heating deepens the boundary layer, diluting surface emissions and entraining free tropospheric air with lower CO_2 concentrations. Concurrently, daytime photosynthetic uptake further reduces near-surface CO_2 (Mitchell et al., 2018). We further evaluate urban–suburban–coastal differences in these processes. At PY, the CO_2 peak occurred at 08:00–09:00, aligning with morning traffic peaks, reflecting dominant anthropogenic influences. CH's peak appeared 1–2 h earlier than PY due to its longitudinal and elevational position, where earlier sunrise accelerates the breakup of the nocturnal stable boundary layer. Both PY and CH reached minima at 16:00–17:00, likely linked to afternoon photosynthetic activity. NS exhibited irregular peak/valley timing.

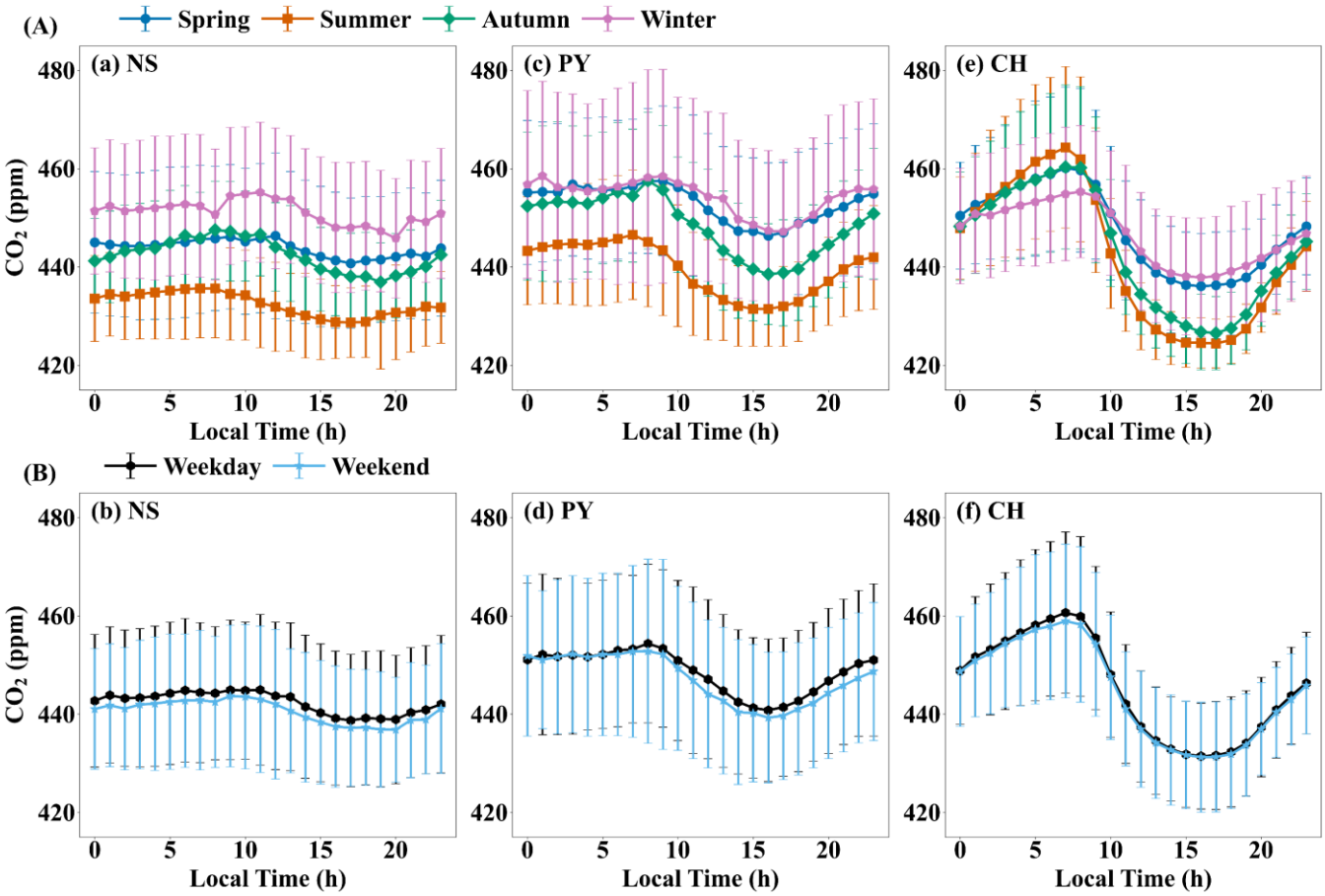

Figure 5. Diurnal CO_2 variations at the (a–b) NS, (c–d) PY, and (e–f) CH stations across (A) seasons and (B) weekdays/weekends. Seasons are defined as Spring (Mar–May), Summer (Jun–Aug), Autumn (Sep–Nov), and Winter (Dec–Feb). Error bars indicate ± 1 SD. The corresponding CO diurnal cycles are shown in Fig. S9.

Diurnal amplitudes at CH and PY were larger in summer/autumn than winter/spring, driven by vegetation activity and boundary layer dynamics (Fig. S8 in the Supplement). Summer/autumn conditions in Guangzhou—abundant light, warmth, and rainfall—optimize vegetation growth, enhancing daytime photosynthesis and nighttime respiration (Dusenge et al., 2019). Optimal canopy temperatures for subtropical evergreen forests (~30 °C) (Liu et al., 2015) align with CH/PY's summer/autumn daytime temperatures (Table S3), explaining their amplified amplitudes. However, the diurnal amplitude of CO_2 at CH in summer and autumn is 2.63 times and 1.77 times that at PY, respectively. The diurnal amplitude of atmospheric CO_2 concentration at CH in summer is 39.90 ppm, which is close to the diurnal amplitude of CO_2 concentration in the suburbs of Hangzhou in summer (35.29 ppm) (Chen et al., 2024). Despite similar temperatures, CH's larger NDVI range and stronger NDVI-CO_2 correlation (−0.72 vs. PY; Figs. 4d and f) highlight greater biogenic dominance, with pronounced daytime uptake and nighttime respiration. NS showed the smallest diurnal amplitudes across seasons (e.g., 5.60 ppm in summer), attributable to sparse vegetation (low NDVI: 0.22–0.42) and frequent summer southerly marine air masses, which dilute coastal CO_2.

Figure 5B contrasts weekday–weekend diurnal CO_2 patterns. All stations generally showed higher weekday concentrations, diverging from Hangzhou and Beijing (Yang et al., 2021; Chen et al., 2024) but aligning with Paris and Boston (Briber et al., 2013; Xueref-Remy et al., 2018). At CH, the daytime weekday–weekend contrast is small. This could reflect a weak anthropogenic weekday–weekend signal relative to other sources of variability, but it does not uniquely diagnose source dominance because transport and boundary-layer mixing may dilute or mask weekday–weekend differences. At PY, the clearer daytime weekend decrease is consistent with reduced on-road activity in the urban core. At NS, weekday CO_2 remains higher across much of the day, which may reflect weekday-intensified construction and port-related logistics in the surrounding area (for example, the Metro Line 18 extension and operations near the Nansha Container Terminal Phase III, ~5 km east), superimposed on transport and mixing effects.

To corroborate the combustion contribution to the CO_2 diurnal cycle, we examined synchronous CO measurements (Fig. S9 in the Supplement). At all sites, CO shows a consistent seasonal ordering (winter highest, summer lowest), and its morning maximum at PY (typically 08:00–10:00) coincides with the CO_2 morning peak (Fig. 5), supporting traffic/combustion control of the early-day enhancement. In contrast to CO_2, CO exhibits only a weak mid-afternoon minimum (including at CH), consistent with CO_2 being additionally depressed by photosynthetic uptake while CO is unaffected; both species remain modulated by transport and boundary-layer mixing. Weekday–weekend differences are small at CH but clearer at PY/NS (Fig. S9), indicating a stronger anthropogenic weekly-cycle imprint in the urban-core and coastal/port settings. Overall, the CO–CO_2 contrast reinforces our interpretation that the morning CO_2 maxima are primarily combustion-driven, whereas the pronounced mid-afternoon CO_2 minima at vegetated sites reflect biogenic uptake rather than reduced emissions.

3.2 Sea–land breeze impacts

Based on meteorological observations from the NS coastal tall tower, 84 sea–land breeze days (SLBD) were identified in Guangzhou between January 2023 and September 2024, accounting for 13.14 % of the monitoring period, with peaks in spring and autumn. These transitional seasons between summer and winter are characterized by weaker synoptic systems and lighter background winds, favoring SLBD occurrence (Mai et al., 2024b). Our results align with SLBD seasonal distributions for the Pearl River Estuary cities of Zhuhai and Guangzhou in 2022 (Zhang et al., 2024; Mai et al., 2024b). Figure 6 compares CO_2 concentrations during SLBD and non-SLB days (NSLBD) across stations. Overall, average CO_2 concentrations during SLBD were lower than during NSLBD by 5.87 ppm at NS, 3.08 ppm at PY, and 0.75 ppm at CH. This indicates that SLB circulation enhances ventilation and

CO_2 dispersion, with the SLBD-related reduction decreasing from the coastal site to the urban core and being smallest at the suburban site (NS > PY > CH). This pattern is similar to SLB-driven dispersion reported for $PM_{2.5}$, PM_{10}, and ozone in Tianjin (Hao et al., 2017). Seasonal differences were pronounced: SLB promoted CO_2 dispersion at NS and PY in spring, winter, and autumn (spring > winter > autumn), but increased CO_2 accumulation in summer. Tianjin similarly observed summer $PM_{2.5}/PM_{10}$ accumulation under SLB (Hao et al., 2017). At CH, SLBD reduced CO_2 in spring, summer, and autumn but increased it in winter, likely due to limited inland SLB penetration and competing winter processes.

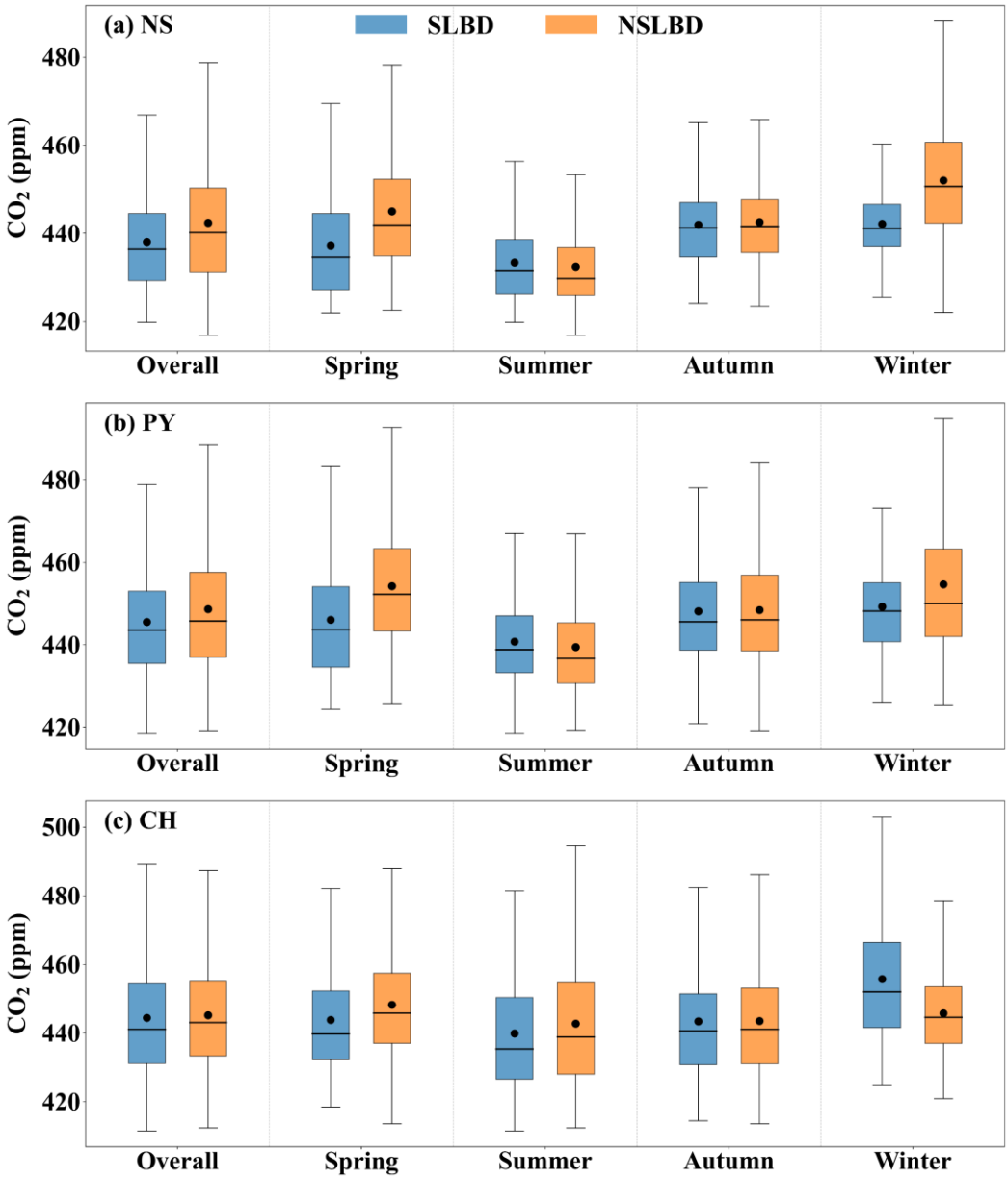

Figure 6. Boxplots of atmospheric CO_2 concentrations (black dots denote means; black line denotes the median) during sea–land breeze days (SLBD) and non-SLB days (NSLBD) by station and season, with outliers excluded.

To resolve seasonal and diurnal SLB impacts, we analyzed CO_2 diurnal variations during SLBD and NSLBD (Fig. 7). Focusing on NS (due to similar PY–NS trends and space constraints), spring and winter SLBD reduced CO_2

concentrations by 7.76 ppm and 9.77 ppm (hourly mean differences), respectively, driven by stronger winds (Fig. 7) and deeper boundary layers (Fig. S10 in the Supplement). Autumn SLB only reduced CO_2 during sea breeze hours (mean difference: 1.69 ppm). Autumn's weaker winds and boundary layers resulted in reduced dispersion compared to spring/winter. In summer, SLB increased CO_2 by 2.08 ppm (sea breeze hours) due to stable atmospheric stratification. Summer temperatures were 6.00 °C and 12.19 °C higher than spring and winter (Table S3), respectively. Under calm, rain-free conditions, the collision of moist marine air with dry-hot coastal land formed a thermal internal boundary layer (TIBL), inducing low-level temperature inversions near the SLB convergence zone (Liu et al., 2001; Reddy et al., 2021). These inversions suppressed horizontal/vertical mixing, trapping CO_2 (Stauffer et al., 2015; Hao et al., 2024). NS's summer SLBD winds averaged 1.05 m s^{-1} (sea breeze) and 0.96 m s^{-1} (land breeze)—38.60 %, 63.16 %, and 15.32 % lower than spring, winter, and autumn winds, respectively—while boundary layer heights (590.54 m) were 9.51 % shallower than NSLBD (Fig. S10). Weak winds and shallow boundary layers stabilized atmospheric stratification, limiting CO_2 dispersion and elevating ground-level CO_2 by up to 4.03 ppm.

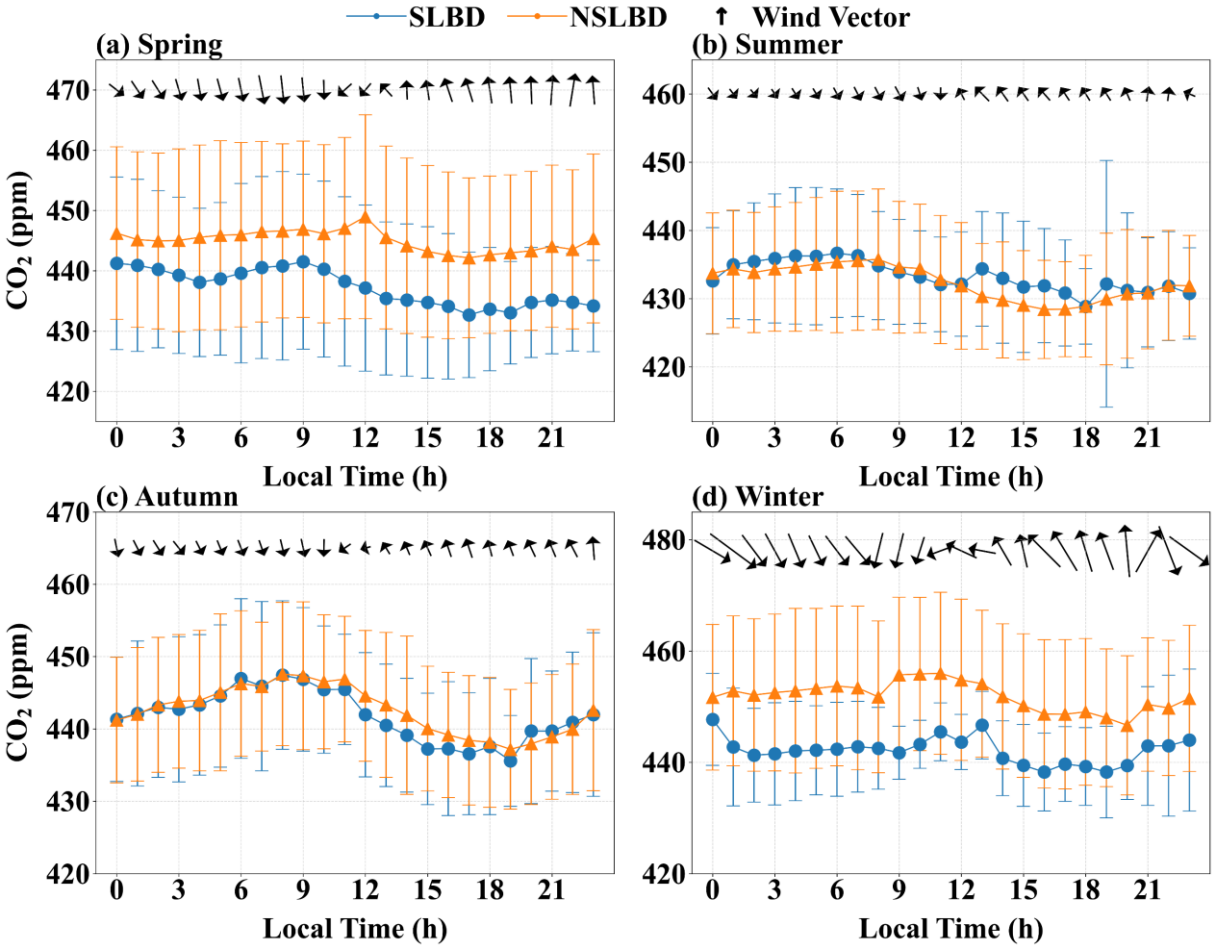

Figure 7. Diurnal variations in CO_2 concentrations, wind direction, and wind speed at the coastal station (NS) during sea–land breeze days (SLBD) and non-SLB days (NSLBD) by season. Error bars indicate ± 1 SD. The corresponding CO diurnal cycles are shown in Fig. S11.

CO provides a combustion-specific tracer to further diagnose SLB modulation of anthropogenic signals (Fig. S11 in the Supplement). In spring and winter, CO is generally lower on SLBD than on NSLBD, consistent with enhanced dilution and export by the breeze circulation, broadly mirroring the CO_2 behavior (Fig. 7). In autumn, the CO response is weaker and transitional, with only modest daytime reductions. In summer, however, SLB days exhibit a pronounced afternoon CO build-up, with a much larger relative enhancement than CO_2 (relative to the seasonal 24 h mean on NSLBD: ~10 % for CO versus ~0.7 % for CO_2), implying trapping/recirculation of fresh combustion plumes under weak-wind, shallow-mixing conditions. Overall, the joint CO–CO_2 behavior confirms that SLB exerts a seasonally varying control on near-surface carbon signals—ventilating in cooler seasons but favoring accumulation under the stagnant summer regime.

3.3 CO_2 enhancements and uncertainties

Figure S12 (in the Supplement) presents the time series of observed CO_2 and CO concentrations at Guangzhou's stations relative to marine backgrounds from January 1 to December 27, 2023. Compared to urban observations with significant hourly variability, marine background concentrations in Guangzhou remained stable, with summer and winter CO_2 standard deviations of 0.94 ppm and 0.67 ppm, respectively, indicating minimal local source/sink influences. Using Eqs. (13) and (14), marine background uncertainties were calculated (Table S4 in the Supplement). Summer and winter CO_2 marine background uncertainties were 0.96 ppm and 0.70 ppm, respectively, constraining urban marine background uncertainties below 1 ppm—slightly lower than Los Angeles's 1.4 ppm (Verhulst et al., 2017). CO marine background uncertainties were 12.68 ppb (summer) and 18.36 ppb (winter).

Based on background concentrations, CO_2 enhancements were derived for all stations. Figure 8 shows enhancements across all hours, afternoon (12:00–16:00), and midnight (00:00–05:00) periods in 2023, summer, and winter. Annual median enhancements were 13.59 (NS), 17.70 (PY), and 16.29 ppm (CH), with pronounced spatiotemporal variability—closely aligning with the 10–20 ppm range observed annually in the Beijing-Tianjin-Hebei (BTH) urban cluster of China (Han et al., 2024). In summer, the all-hours enhancement followed a south-to-north gradient: 7.00 (NS), 13.23 (PY), and 16.91 ppm (CH). This inland maximum likely reflects the combined influence of coastal transport, biogenic exchange, and boundary-layer mixing, and is consistent with the seasonal gradient displacement discussed in Sect. 3.1 (Fig. 3). Afternoon enhancements peaked at PY (6.92 ppm), whereas midnight enhancements at CH reached 31.36 ppm. Winter afternoon enhancements reversed this pattern: 16.58 (NS), 12.37 (PY), and 7.45 ppm (CH), with NS and PY values 4.39 times and 1.79 times higher than summer. Midnight enhancements at CH remained highest in winter (18.87 ppm), despite a 38.93 % reduction from summer.

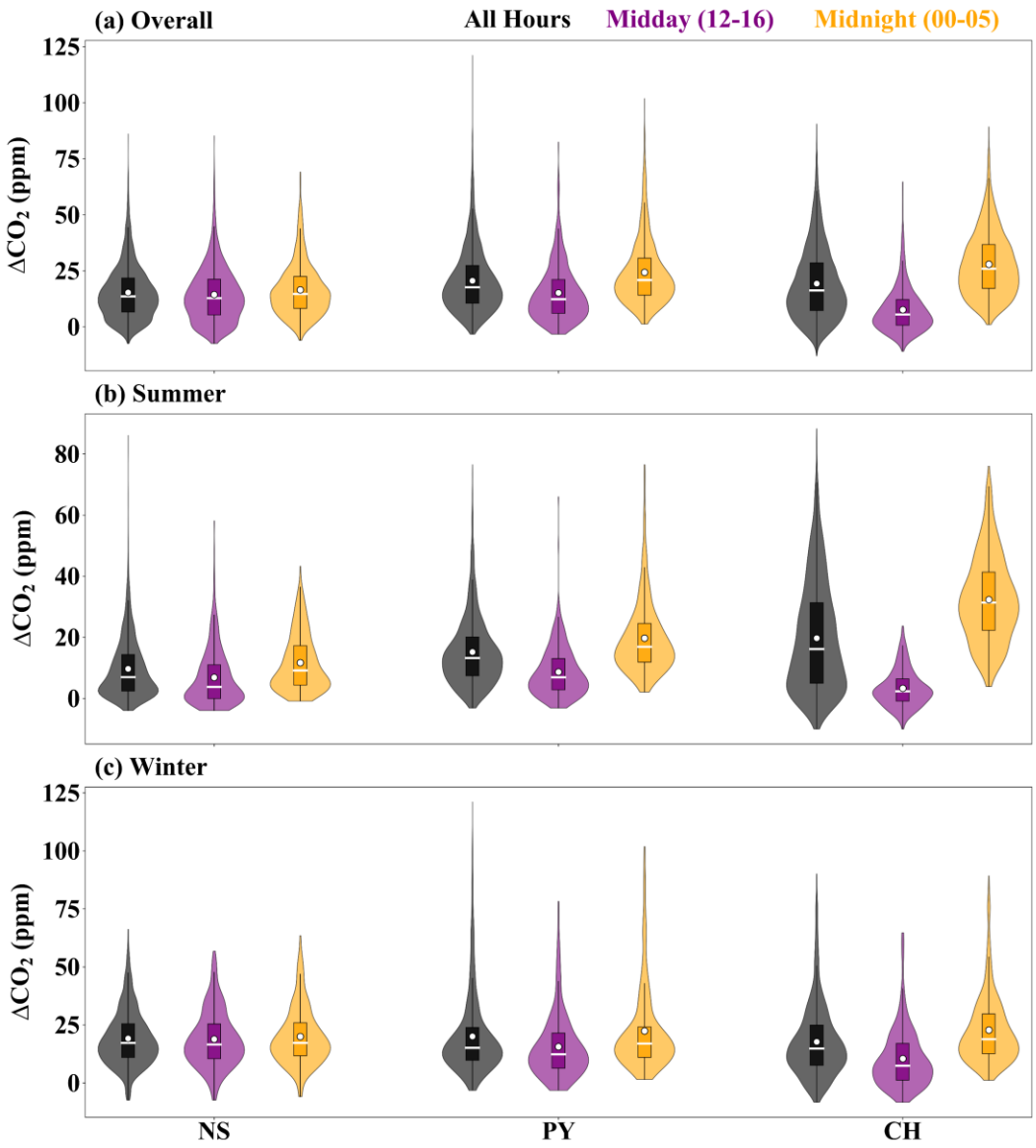

Figure 8. Distributions of hourly CO_2 enhancement (ΔCO_2) above the background concentrations at NS, PY, and CH during the (a) overall, (b) summer, and (c) winter periods, shown for all hours, midday (12:00–16:00 LT), and midnight (00:00–05:00 LT). White dots denote the mean values, and white horizontal lines denote the median values.

This spatiotemporal variability reflects divergent influences of anthropogenic emissions, biogenic fluxes, and atmospheric mixing. At CH, strong diurnal shifts in enhancements (e.g., 31.36 ppm summer midnight) highlight biogenic dominance, with long-tailed distributions (Fig. 8). Stable, shallow nighttime boundary layers trapped respiratory emissions near the surface, consistent with isotopic studies in Xi'an (32.80 ppm) and Switzerland (30.00 ppm) (Wang et al., 2021; Berhanu et al., 2017). At NS, transport dominated: summer southerly marine air masses reduced enhancements, while winter northerly winds transported urban emissions downstream, raising NS enhancements to PY levels (exceeding PY in afternoons). PY's enhancements were primarily anthropogenic, validated by CO co-variation. CO, a tracer for combustion-derived CO_2, showed significantly higher concentrations at PY (Fig. S12). PY's median midnight CO enhancements in summer were 2.04 times and 1.43 times higher than

NS and CH (Fig. S13 in the Supplement). Shallow nocturnal boundary layers localized anthropogenic CO near the surface, with minimal vertical/horizontal transport, confirming PY's anthropogenic dominance.

3.4 Continuous observations of $\Delta CO/\Delta CO_2$ ratios

Reduced Major Axis regression (Model II) was applied to analyze the relationship between CO (ΔCO) and CO_2 (ΔCO_2) concentration enhancements across stations, with the $\Delta CO/\Delta CO_2$ emission ratio (R_{CO}) derived from regression slopes (Fig. 9). In 2023, R_{CO} values for NS, PY, and CH were 8.48 ± 1.81, 7.45 ± 1.38, and 4.16 ± 3.59 ppb ppm^{-1}, respectively, with correlation coefficients of 0.78, 0.72, and 0.33, indicating significant spatiotemporal heterogeneity. Summer R_{CO} was generally lower than winter, with CH exhibiting the lowest seasonal value (2.66 ± 0.83 ppb ppm^{-1}). Winter maxima occurred at NS (11.03 ± 1.49 ppb ppm^{-1}), followed by PY (9.08 ± 1.13 ppb ppm^{-1}) and CH (8.56 ± 1.82 ppb ppm^{-1}).

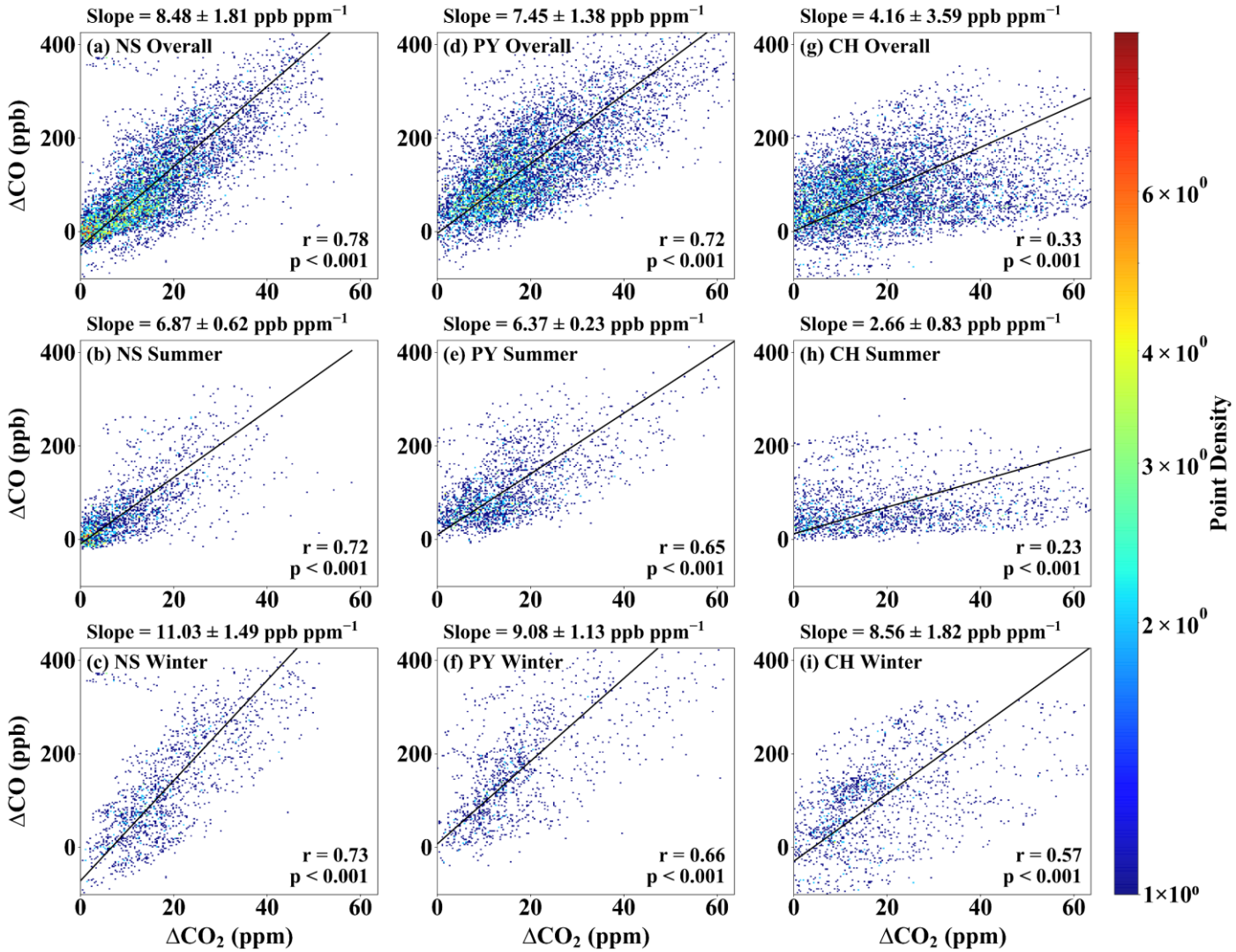

Figure 9. Seasonal relationships between ΔCO_2 and ΔCO enhancements at the (a–c) NS, (d–f) PY, and (g–i) CH stations, analyzed using geometric-mean regression. Panels are shown as 2D histogram density plots (hist2d; 200 × 200 bins), where color indicates the number of paired observations per bin. The fitted slope represents the $\Delta CO/\Delta CO_2$ emission ratio (R_{CO}; ppb ppm^{-1}), reported as mean ± 1 SD (reflecting temporal variability).

570 Comparatively, Beijing's urban R_{CO} in 2019 was measured at 10.46 ± 0.11 ppb ppm^{-1} using portable Fourier-
571 transform spectroscopy (Che et al., 2022a), while Shanghai and Los Angeles showed 10.22 ± 0.40 and 9.64 ± 0.46
572 ppb ppm^{-1}, respectively, based on satellite and model data (Wu et al., 2022a). Guangzhou's lower R_{CO} is consistent
573 with the post-2013 tightening of China's air-quality management across the energy and transport sectors, rather
574 than a single intervention. National action plans (2013–2017 Air Pollution Prevention and Control Action Plan;
575 2018–2020 Three-Year "Blue-Sky" Action Plan) strengthened coal/industrial and vehicle-emission controls with
576 explicit targets and timelines. In parallel, ultra-low-emission (ULE) retrofits of coal-fired power units were rolled
577 out through 2020, and China 6 (VI) on-road emission standards were phased in, with large cities (including
578 Guangzhou) leading implementation; Guangdong's provincial Blue-Sky measures further reinforced
579 industrial/mobile-source controls and promoted fleet electrification. These measures coincide with independent
580 inventory evidence of declining national CO emissions (~23 % during 2013–2017) (Zheng et al., 2018), plausibly
581 reducing CO/CO_2 emission ratios from dominant urban sources. Consistently, Beijing's R_{CO} decreased from > 30
582 ppb ppm^{-1} in 2006 (Han et al., 2009) to 10.22 ± 0.40 ppb ppm^{-1} by 2020 (Wu et al., 2022a), with additional
583 reductions during the 2008 Olympics and 2020 COVID-19 lockdowns (Wang et al., 2010; Cai et al., 2021). In
584 Guangdong, restrictions on coal plants, retirement of inefficient industries, and promotion of electric vehicles
585 coincided with large declines in SO_2 and NO_2 (85 % and 35 % in 2019 relative to 2006) (Hu et al., 2021), and Mai
586 et al. (2021) likewise reported improved combustion efficiency in the PRD associated with advances in gasoline
587 vehicles. We emphasize that this interpretation is consistency-based rather than a formal causal identification; fuel
588 mix, fleet composition, and atmospheric oxidation may also contribute (Young et al., 2023; Vimont et al., 2019).
589
590 Seasonal R_{CO} variations stem from biogenic exchange and transport dynamics. Summer's weaker $\Delta CO–\Delta CO_2$
591 correlations at CH reflect dominant biogenic influences (daytime uptake and nighttime respiration), as reported in
592 Beijing, Indianapolis, and Switzerland (Turnbull et al., 2015; Berhanu et al., 2017; Che et al., 2022a). Biogenic
593 impacts decreased from suburban > urban > coastal, aligning with vegetation gradients. Winter's higher R_{CO} at CH
594 and NS correlated with reduced biogenic activity and northerly transport of urban emissions under stable boundary
595 layers. Berhanu et al. (2017) attributed winter R_{CO} increases to cold-air advection and boundary layer accumulation.
596 NS's winter R_{CO} (4.16 ppb ppm^{-1} higher than summer) linked to urban airmass origins, while PY's seasonal shifts
597 reflected suburban source–sink variations. Although secondary CO from upwind Volatile Organic Compounds
598 (VOCs) and CH_4 oxidation could perturb R_{CO}, their combined contribution was merely 1 % in coastal urban regions
599 (Griffin et al., 2007).

3.5 Partitioning anthropogenic and biogenic fluxes

Section 3.4 shows that the sites differ in how well the $\Delta CO–\Delta CO_2$ relationship reflects fossil-fuel combustion. At CH, especially in summer, CO_2 variability is strongly influenced by biogenic exchange, which weakens the combustion linkage implied by R_{CO} and can bias an R_{CO}-based fossil-fuel estimate. At NS, in contrast, variability is dominated by changing transport and upwind airmass origin, particularly in winter when urban plumes frequently reach the coastal site. We therefore select PY—the urban-core site with a comparatively robust combustion signal—to quantify the surface CO_2 emissions (CO_2tot) constrained by the observed concentration enhancements and footprint-informed transport. Using the PY-specific R_{CO}, we then partition CO_2tot into fossil-fuel (CO_2ff) and biogenic (CO_2bio) components.

Figure 10 summarizes mean afternoon (12:00–16:00 LT) CO_2tot, CO_2ff, and CO_2bio at PY for July 2023 (summer) and December 2023 (winter). Bars show monthly means of daily afternoon values. The plotted error bars indicate ± 1 standard deviation (SD) across days and thus represent day-to-day variability in ventilation, mixing, and transport rather than uncertainty of the monthly mean. Mean uncertainty is quantified by the standard error (SE), which is distinct from the SD shown in Fig. 10. In July, CO_2tot = 2.38 ± 0.45, CO_2ff = 5.97 ± 0.75, and CO_2bio = −3.59 ± 0.63 μmol m^{-2} s^{-1} (mean ± SE), whereas in December CO_2tot = 13.50 ± 2.20, CO_2ff = 13.56 ± 2.40, and CO_2bio = −0.06 ± 1.13 μmol m^{-2} s^{-1} (Table S5). Because CO_2bio is diagnosed as a residual (CO_2bio = CO_2tot − CO_2ff), its uncertainty reflects propagated uncertainties from both CO_2tot and CO_2ff—including measurement and background-selection uncertainty and R_{CO}-related variability—rather than being independent. Notably, December CO_2bio is close to zero. The bootstrap 95 % CI of the monthly mean is [−2.28, 2.09] μmol m^{-2} s^{-1}, which includes zero, indicating that the net biogenic flux was not statistically distinguishable from zero during winter afternoons, likely reflecting a near-neutral balance between photosynthesis and respiration. In contrast, the July mean CO_2bio remains clearly negative relative to its uncertainty, supporting robust summertime net biogenic uptake despite uncertainty propagation inherent to the residual calculation. When assessed using daily afternoon means, the July–December contrasts are statistically significant for CO_2tot, CO_2ff, and CO_2bio (Welch and Mann–Whitney tests; bootstrap 95 % confidence intervals; Table S5). Robust distributional metrics corroborate this significant seasonal increase despite partial day-to-day overlap: the CO_2ff median increases from 4.33 (IQR: 3.58–7.81) in July to 10.70 (IQR: 6.74–18.28) μmol m^{-2} s^{-1} in December. Across both months, CO_2ff is larger in magnitude than CO_2bio, implying that the PY afternoon enhancement is primarily fossil-fuel driven, consistent with fossil-dominated urban enhancements reported for other Chinese cities (Wang et al., 2022). The stronger winter CO_2ff relative to summer is explained mainly by atmospheric dynamics—reduced dilution under weaker marine ventilation and a shallower

boundary layer—while seasonal emission changes (e.g., winter residential energy use) likely provide a secondary contribution. In contrast, CO_2bio is more negative in summer, consistent with higher summer NDVI (+11 %) and warmer conditions approaching optimal canopy temperatures (Table S3).

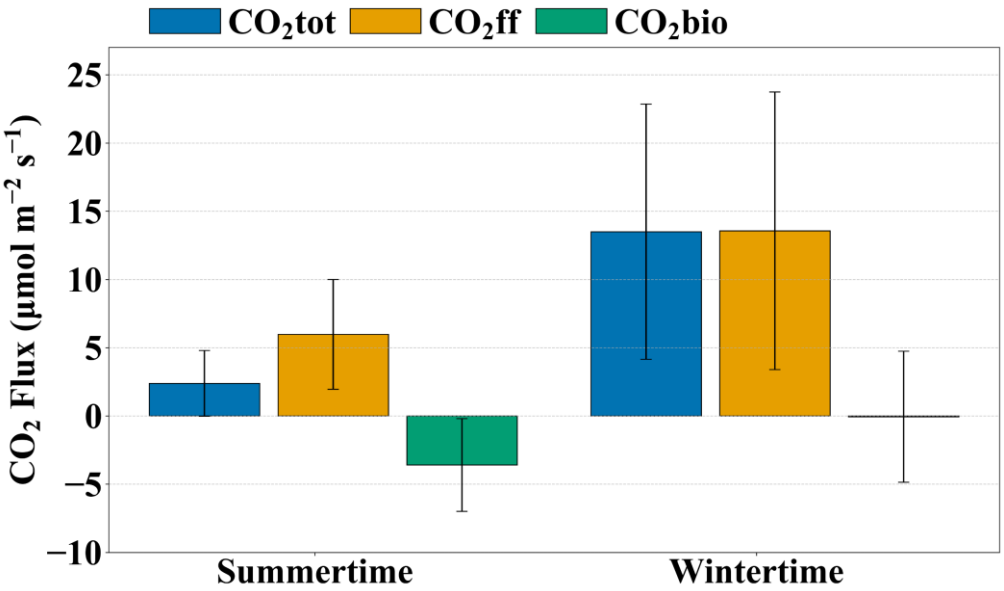

Figure 10. Average afternoon (12:00–16:00 LT) CO_2tot, CO_2ff, and CO_2bio at PY for July 2023 (summer; n = 29 valid days) and December 2023 (winter; n = 18 valid days). December has fewer valid days because objective QC excluded days with incomplete afternoon coverage (e.g., instrument downtime/maintenance), so the smaller winter sample reflects data availability rather than subjective selection. Bars show monthly means of daily afternoon values. Error bars indicate ± 1 standard deviation (SD) across daily afternoon means within each month (day-to-day atmospheric variability), not the standard error (SE) of the monthly mean; SE and confidence intervals are reported in Table S5.

To test the robustness of the winter fossil-fuel dominance inferred at PY—when combustion signals are strongest—we reran the winter flux-estimation workflow using paired daily afternoon means (12:00–16:00 LT). We then varied (1) particle number (1000/2000), (2) grid spacing (0.05°/0.10°), and (3) backward duration (96/120 h) relative to the baseline (500 particles, 0.08°, 72 h). Mean changes were small for both components (Table S6 in the Supplement; Fig. 11A). Increasing particle number to 1000/2000 changed CO_2ff by −0.56 %/−0.24 % and CO_2tot by −0.52 %/−0.31 %. Refining the grid to 0.05° yielded comparably small decreases (CO_2ff: −0.72 %; CO_2tot: −0.78 %). Extending the backward duration to 96/120 h produced changes of −1.34 %/−1.05 % for CO_2ff and −1.33 %/−1.31 % for CO_2tot. Only the coarser 0.10° grid produced a statistically detectable, yet small, decrease (CO_2ff: −1.47 %, $p = 0.0269$; CO_2tot: −1.40 %, $p = 0.0164$). All other settings yielded changes ≤1.34 % with 95 % CIs spanning zero ($p \geq 0.083$), indicating no evidence of material bias at our sample size. Day-to-day consistency remained essentially unchanged across settings, with extremely high correlations (CO_2ff: $r = 0.9993$–0.9997; CO_2tot: $r = 0.9992$–0.9997) and small RMSE values (CO_2ff: 0.31–0.45 μmol m^{-2} s^{-1}; CO_2tot: 0.28–0.45 μmol m^{-2} s^{-1}), consistent with the near-1:1 paired scatter (Fig. 11B). Because wintertime CO_2bio at PY was close to zero,

percent differences were not informative; in absolute terms, test–baseline differences in CO_2bio remained small (order 10^{-2} μmol m^{-2} s^{-1}) with 95 % CIs generally spanning zero, consistent with the tight across-run daily spread (median 0.045 μmol m^{-2} s^{-1}; IQR 0.016–0.067 μmol m^{-2} s^{-1}) (Table S7 in the Supplement). Across the baseline plus six variants, the day-by-day ensemble spread was tightly bounded (median 0.20–0.21 μmol m^{-2} s^{-1}, median CV ≈ 1.8 %). Together, these results indicate that our baseline STILT configuration lies in a converged regime and that the inferred winter CO_2ff dominance is robust to reasonable transport-parameter choices.

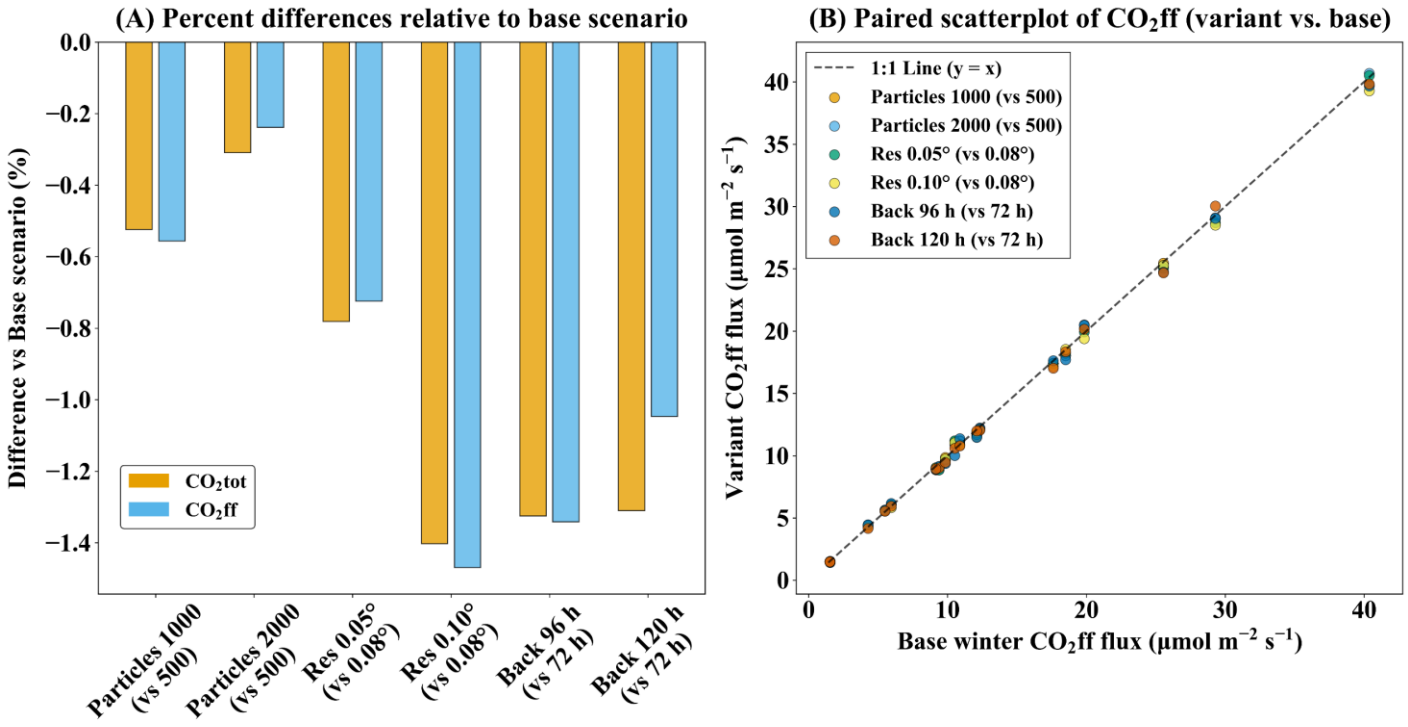

Figure 11. STILT parameter sensitivity at PY (winter). Panel A: mean percent difference (variant − baseline) of inferred fluxes relative to the winter baseline (500 particles, 0.08°, 72 h), computed from paired daily afternoon means (12:00–16:00 LT; n = 18); Δ% = (variant − base)/base × 100; negative values indicate lower than baseline. Panel B: paired scatter of CO_2ff (μmol m^{-2} s^{-1}) from each variant versus the baseline for the same days; solid line is 1:1 (y = x).

For winter afternoons at PY, measurement and background-selection uncertainties—estimated by propagating their combined enhancement uncertainty through Eqs. (12)–(14)—contribute only ~0.36 μmol m^{-2} s^{-1}, i.e., ~3 % of the mean winter-afternoon CO_2ff. Paired-day STILT sensitivity tests (Fig. 11) further indicate that the winter-afternoon CO_2ff attribution is robust to reasonable transport-parameter choices. The remaining uncertainty is thus more likely dominated by residual transport representation error and coastal mesoscale flow (e.g., wind and boundary-layer mixing biases), as documented for winter conditions in meteorological/transport modeling (Yadav et al., 2021; Lin et al., 2021). To provide independent context, we benchmark our winter-afternoon estimate against bottom-up inventories, which are used solely for contextual comparison and do not enter the CO_2 partitioning. We use 2023 inventories at 0.1° × 0.1° resolution, temporally disaggregate annual totals to hourly emissions using the same profiles (Crippa et al., 2020), and compute the winter-afternoon (12:00–16:00 LT) mean emission flux over the

winter footprint-defined sensitivity region (Fig. 12). This yields 19.81 μmol m^{-2} s^{-1} from the EDGAR_2024_GHG (2023) inventory (Crippa et al., 2024) and 85.46 μmol m^{-2} s^{-1} from the MEIC-global-CO_2 (2023) inventory (Xu et al., 2024). While this aligns qualitatively with higher MEIC estimates reported for Guangdong Province (Yang et al., 2025), the contrast is larger for our winter-afternoon sensitivity region. This likely reflects differences in spatial disaggregation and point-source representation (e.g., road-network allocation and power-plant locations) that can be accentuated at sub-provincial scales (Yang et al., 2025).

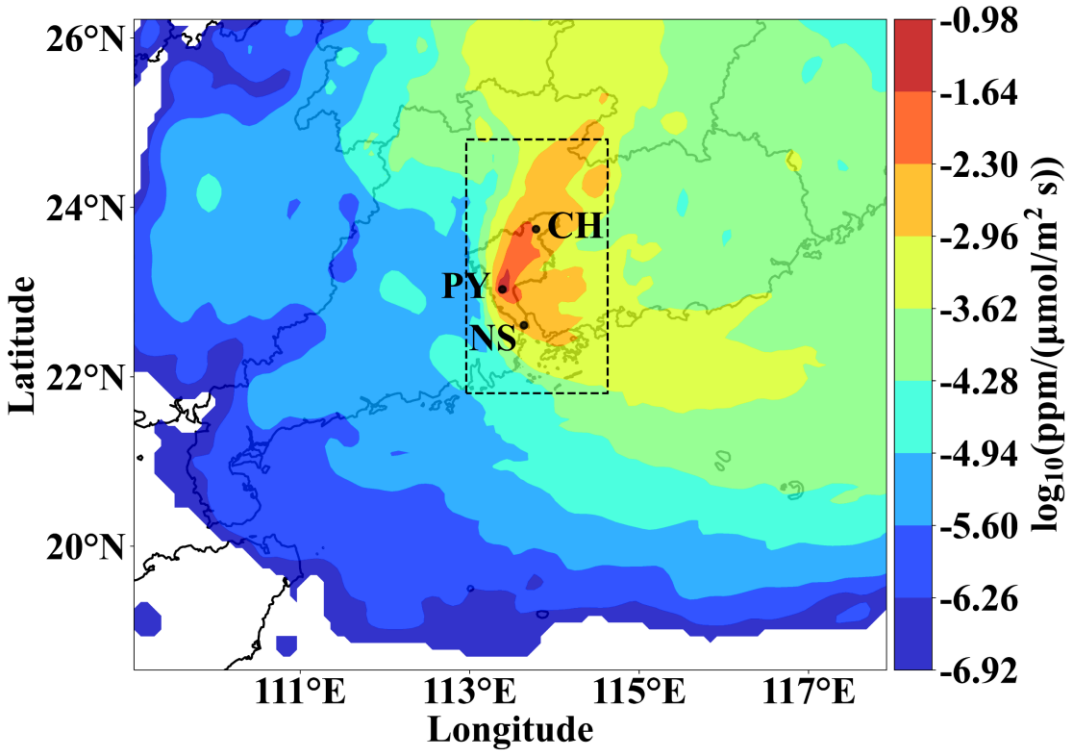

Figure 12. Spatial distribution of the mean winter-afternoon (12:00–16:00 LT) STILT footprint at the PY station, representing the receptor sensitivity to upwind surface fluxes. Colors denote the log10-transformed footprint sensitivity (ppm per (μmol m^{-2} s^{-1})). The dashed rectangle outlines the sensitivity region used for inventory flux aggregation and benchmarking in Sect. 3.5.

Notably, our observation-based CO_2ff reflects the footprint-weighted enhancement sampled at PY during winter afternoons after background removal, whereas inventories provide gridded emission fields from which an unweighted domain-mean afternoon flux can be computed over the sensitivity region. Because only grid cells with substantial STILT footprint influence contribute materially to the receptor enhancement—and these weights are highly heterogeneous and transport-dependent (Fig. 12)—the unweighted domain-mean inventory flux may be non-uniformly represented in the receptor signal under variable coastal transport (Gerbig et al., 2003; Lin et al., 2003; Fasoli et al., 2018). Accordingly, an effective footprint-weighted mean flux estimate inferred from the receptor enhancement can differ from the unweighted afternoon-mean inventory flux over the sensitivity region. This difference depends on the spatial alignment between heterogeneous transport footprints and spatially heterogeneous

emissions (including localized hotspots), because under a given transport regime many grid cells within the domain may carry negligible footprint influence (Hüser et al., 2017; Kunik et al., 2019). We therefore interpret inventory comparisons as a plausibility envelope that reflects inter-inventory spread, rather than a validation target. Such inventory–observation differences are also reported for other coastal urban basins (e.g., Los Angeles) and are often sensitive to boundary-layer representation and meteorological inputs (Kim et al., 2025).

Beyond the winter fossil-fuel benchmark above, we further place the summer biogenic component and its offset ratio in the context of independent regional and urban estimates. Summer afternoons exhibited mean CO_2bio of -3.59 ± 0.63 μmol m^{-2} s^{-1}, consistent with observation-based Pearl River Delta NEE (−0.1 to −12 μmol m^{-2} s^{-1}) (Mai et al., 2024a), and with modeled urban biogenic flux ranges (0 to −15 μmol m^{-2} s^{-1}) reported in previous studies (Wu et al., 2021; Wei et al., 2022; Kim et al., 2025). Consequently, summer-afternoon biogenic uptake offsets 60.13 % of concurrent CO_2ff at PY, with a bootstrap 95 % confidence interval of 48–72 %, highlighting substantial biogenic modulation of coastal urban CO_2 signals. Importantly, the inferred summertime offset remains substantial within the estimated uncertainty range, indicating robust biogenic modulation in magnitude. Comparable growing-season offsets have been reported for other coastal urban regions using independent approaches. A sensor-network combined with box-model analysis for Los Angeles suggests up to 60 % daytime offset; an inversion for the Boston coastal region indicates >50 % summer-afternoon offset (Kim et al., 2025; Sargent et al., 2018). High-resolution vegetation modeling for New York City similarly suggests ~40 % offset of afternoon anthropogenic enhancements and the potential to fully balance on-road traffic contributions (Wei et al., 2022). Overall, these contextual comparisons provide an external plausibility check and indicate that strong growing-season biogenic uptake is a plausible and important modulator of coastal-urban CO_2 signals in Guangzhou.

4 Conclusions

Three key knowledge gaps still limit the interpretation of atmospheric CO_2 signals in coastal megacities and their use for mitigation-relevant assessment. To address them, we present an observation-driven framework—without assimilating emission inventories—that combines multi-site CO_2/CO measurements, footprint-informed transport analysis, and a site-specific $\Delta CO/\Delta CO_2$ (R_{CO}) relationship to interpret coastal megacity CO_2 dynamics in Guangzhou (January 2023–September 2024). Relative to prior studies, this framework provides a distinct, process-based view of spatiotemporal CO_2 variability, sea–land breeze (SLB) modulation, and source–sink partitioning in a coastal setting. The three-site gradient reveals contrasting dominant controls by setting: transport governs the largest seasonal amplitude at the coastal site, biogenic exchange drives pronounced summertime daytime

drawdown at the vegetated site, and combustion dominates variability in the urban core. This combustion signal is characterized by a regression-derived R_{CO}, which is consistent with the broad post-2013 shift toward cleaner fuels and stringent vehicle emission standards in the Pearl River Delta. Importantly, these patterns point to a seasonally displaced coastal CO_2 "dome". In contrast to the traditional paradigm where the maximum CO_2 enhancement is anchored over the urban center, our results demonstrate that in coastal megacities the dome's peak can be displaced from the urban core by the combined effects of seasonal coastal transport/mixing and seasonally varying biogenic uptake associated with urban greening, underscoring the dynamic nature of coastal greenhouse gas distributions.

Under prevailing fair-weather coastal mesoscale conditions, the SLB circulation exerts a key control on diurnal variability in near-surface CO_2 and CO, with a non-linear seasonal modulation. In spring and winter, SLB strengthens ventilation and lowers CO_2, whereas in summer it can favor accumulation (+2.08 ppm during sea-breeze hours) under weak-wind, stable conditions. Consistent with this, CO exhibits a more pronounced daytime enhancement than CO_2 during summer SLB days, supporting a trapping/recirculation regime in which combustion plumes are retained when coastal mesoscale flows coincide with shallow mixing and stable stratification. These seasonally opposing SLB impacts may be overlooked because many urban CO_2 studies focus on inland settings or annual-mean signals. Our results show that coastal mesoscale circulations can reverse the sign of SLB effects across seasons, highlighting important implications for inversion design and interpretation in coastal cities.

Source–sink attribution results at PY indicate that winter-afternoon CO_2ff in the urban core is robust within the quantified measurement and background-selection uncertainty (~3 % of the mean CO_2ff) and shows only small sensitivity to transport-model configurations (≤1.47 % across the tested STILT setups), supporting stable winter-afternoon attribution under our sampling and background definition. In summer afternoons, the inferred CO_2bio (-3.59 ± 0.63 μmol m^{-2} s^{-1}) indicates substantial biogenic uptake that offsets a large fraction (~60 %) of the concurrent fossil contribution during the peak growing season, and this offset remains substantial within the estimated uncertainty bounds. The inferred summertime offset is broadly consistent with independent estimates reported for other coastal urban regions, providing an external plausibility check on the inferred source–sink separation.

Several limitations remain. The three-site network cannot resolve hyperlocal source heterogeneity, and SLB identification relies on near-surface wind criteria rather than full 3-D boundary-layer structure. Although configuration sensitivity is small, transport uncertainties associated with winds and boundary-layer mixing are not

fully quantified here. In addition, CO-based attribution is sensitive to variability in R_{CO} arising from changing source mix, plume processing, and background definition, which propagates into CO_2ff and the residual CO_2bio. Future work combining denser low-cost networks, boundary-layer profiling, and periodic isotopic constraints would further tighten coastal urban carbon budgets.

Overall, our results demonstrate that coastal mesoscale dynamics can reshape both the magnitude and interpretation of urban CO_2 signals, with SLB acting as ventilation in cool seasons but as a trapping/recirculation mechanism in summer under weak-wind stability. The substantial summertime biogenic offset further indicates that biogenic exchange associated with urban greening can materially modulate apparent fossil-fuel signals and should be accounted for when interpreting mitigation trends. These findings have direct implications for coastal urban monitoring and policy evaluation: to avoid season-dependent biases in assessing mitigation progress, urban monitoring networks should prioritize the decoupling of biogenic signals—particularly during summer—to accurately isolate anthropogenic contributions and thus ensure the robust evaluation of urban mitigation progress. Furthermore, the strategic selection of monitoring sites in coastal megacities must explicitly account for the non-linear accumulation effects of SLB circulations to ensure long-term sampling representativeness. While our framework does not produce posterior flux fields as in a formal Bayesian inversion, it provides a complementary, observation-driven tool for rapid process attribution and consistency checking in coastal urban carbon monitoring and mitigation assessment.

Code and data availability. The STILT model source code used in this paper has been published on Zenodo and can be accessed at https://doi.org/10.5281/zenodo.1196561 (Fasoli, 2018). The EDGAR data used in this study are publicly available at https://edgar.jrc.ec.europa.eu/dataset_ghg2024#conditions (last access: 18 June 2025)(Crippa et al., 2024). The planetary boundary layer height data used in this study are available at https://doi.org/10.24381/cds.adbb2d47 (Hersbach, 2023). The NDVI data used in this study are available at https://doi.org/10.5067/MODIS/MOD13A3.006 (Didan, 2015). The CarbonTracker (CT-NRT.v2024-5) products are available online at https://doi.org/10.15138/ATPD-K925 (Jacobson et al., 2024). The NOAA Earth System Research Laboratory/Global Monitoring Laboratory (NOAA GML) data used in this study are available at https://doi.org/10.25925/20241101 (Schuldt et al., 2024). Additional data and information used in this study are available from the corresponding author upon request.

Author contributions. JWZ and ML designed the study. JWZ, YJL, CLP, BH, YYH, XFL, SJS, CLC, CW, ZZ, JJL and ML contributed to data collection and data analysis. JWZ designed and performed the model simulations. JWZ and ML wrote the paper with contributions from all coauthors. JJL and SJS provided valuable feedback and opinions for paper refinement. All the authors revised the paper and edited the text.

Competing interests. The contact author has declared that none of the authors has any competing interests.

Disclaimer. Publisher's note: Publisher's note: Copernicus Publications remains neutral with regard to jurisdictional claims in published maps and institutional affiliations.

Acknowledgements. The authors would like to thank the personnel who participated in data collection, instrument maintenance, and logistic support during the field campaign. We also acknowledge the NOAA GML for providing the CO_2 GLOBALVIEWplus v10.1 ObsPack and CarbonTracker CT-NRT.v2024-5 datasets, which were used for monitoring comparison in this study. CarbonTracker CT-NRT.v2024-5 results provided by NOAA GML, Boulder, Colorado, USA from the website at http://carbontracker.noaa.gov.

Financial support. This work was financially supported by the National Natural Science Foundation of China (Grant no. 42477273) and the National Key R&D Program of China (Grant no. 2022YFE0209500).

References

Ahmadov, R., Gerbig, C., Kretschmer, R., Koerner, S., Neininger, B., Dolman, A., and Sarrat, C.: Mesoscale covariance of transport and CO_2 fluxes: Evidence from observations and simulations using the WRF‐VPRM coupled atmosphere‐biosphere model, J. Geophys. Res.-Atmos., 112, https://doi.org/10.1029/2007JD008552, 2007.

Allouche, M., Bou‐Zeid, E., and Iipponen, J.: The influence of synoptic wind on land–sea breezes, Quarterly Journal of the Royal Meteorological Society, 149, 3198-3219, https://doi.org/10.1002/qj.4552, 2023.

Atkins, N. T. and Wakimoto, R. M.: Influence of the synoptic-scale flow on sea breezes observed during CaPE, Monthly weather review, 125, 2112-2130, https://doi.org/https://doi.org/10.1175/1520-0493(1997)125<2112:IOTSSF>2.0.CO;2, 1997.

Berhanu, T. A., Szidat, S., Brunner, D., Satar, E., Schanda, R., Nyfeler, P., Battaglia, M., Steinbacher, M., Hammer, S., and Leuenberger, M.: Estimation of the fossil fuel component in atmospheric CO_2 based on radiocarbon measurements at the Beromünster tall tower, Switzerland, Atmos. Chem. Phys., 17, 10753-10766, https://doi.org/10.5194/acp-17-10753-2017, 2017.

Boon, A., Broquet, G., Clifford, D. J., Chevallier, F., Butterfield, D. M., Pison, I., Ramonet, M., Paris, J.-D., and Ciais, P.: Analysis of the potential of near-ground measurements of CO_2 and CH_4 in London, UK, for the monitoring of city-scale emissions using an atmospheric transport model, Atmos. Chem. Phys., 16, 6735-6756, https://doi.org/10.5194/acp-16-6735-2016, 2016.

Briber, B. M., Hutyra, L. R., Dunn, A. L., Raciti, S. M., and Munger, J. W.: Variations in atmospheric CO_2 mixing ratios across a Boston, MA urban to rural gradient, Land, 2, 304-327, https://doi.org/10.3390/land2030304, 2013.

Cai, Z., Che, K., Liu, Y., Yang, D., Liu, C., and Yue, X.: Decreased anthropogenic CO_2 emissions during the COVID-19 pandemic estimated from FTS and MAX-DOAS measurements at urban Beijing, Remote Sens-basel., 13, 517, https://doi.org/10.3390/rs13030517, 2021.

Che, K., Liu, Y., Cai, Z., Yang, D., Wang, H., Ji, D., Yang, Y., and Wang, P.: Characterization of regional combustion efficiency using ΔXCO: ΔXCO_2 observed by a portable Fourier-Transform Spectrometer at an urban site in Beijing, Adv. Atmos. Sci., 39, 1299-1315, https://doi.org/10.1007/s00376-022-1247-7, 2022a.

Che, K., Cai, Z., Liu, Y., Wu, L., Yang, D., Chen, Y., Meng, X., Zhou, M., Wang, J., Yao, L., and Wang, P.: Lagrangian inversion of anthropogenic CO_2 emissions from Beijing using differential column measurements, Environ. Res. Lett., 17, https://doi.org/10.1088/1748-9326/ac7477, 2022b.

Chen, Y., Ma, Q., Lin, W., Xu, X., Yao, J., and Gao, W.: Measurement report: Long-term variations in carbon monoxide at a background station in China's Yangtze River Delta region, Atmos. Chem. Phys., 20, 15969-15982, https://doi.org/10.5194/acp-20-15969-2020, 2020.

Chen, Y., Lu, Y., Qi, B., Ma, Q., Zang, K., Lin, Y., Liu, S., Pan, F., Li, S., and Guo, P.: Atmospheric CO_2 in the megacity

Hangzhou, China: Urban-suburban differences, sources and impact factors, Sci. Total Environ., 926, 171635, https://doi.org/10.1016/j.scitotenv.2024.171635, 2024.

Corro, L. M., Bagstad, K. J., Heris, M. P., Ibsen, P. C., Schleeweis, K. G., Diffendorfer, J. E., Troy, A., Megown, K., and O'Neil-Dunne, J. P. M.: An enhanced national-scale urban tree canopy cover dataset for the United States, Sci Data, 12, 490, https://doi.org/10.1038/s41597-025-04816-0, 2025.

Crippa, M., Solazzo, E., Huang, G., Guizzardi, D., Koffi, E., Muntean, M., Schieberle, C., Friedrich, R., and Janssens-Maenhout, G.: High resolution temporal profiles in the Emissions Database for Global Atmospheric Research, Scientific Data, 7, https://doi.org/10.1038/s41597-020-0462-2, 2020.

Crippa, M., Guizzardi, D., Pisoni, E., Solazzo, E., Guion, A., Muntean, M., Florczyk, A., Schiavina, M., Melchiorri, M., and Hutfilter, A. F.: Global anthropogenic emissions in urban areas: patterns, trends, and challenges, Environ. Res. Lett., 16, https://doi.org/10.1088/1748-9326/ac00e2, 2021.

Crippa, M., Guizzardi, D., Pagani, F., Banja, M., Muntean, M., Schaaf, E., Monforti-Ferrario, F., Becker, W. E., Quadrelli, R., Risquez Martin, A., Taghavi-Moharamli, P., Köykkä, J., Grassi, G., Rossi, S., Melo, J., Oom, D., Branco, A., San-Miguel, J., Manca, G., Pisoni, E., Vignati, E., and Pekar, F.: GHG emissions of all world countries, Publications Office of the European Union, https://doi.org/10.2760/4002897, 2024.

Deng, A., Lauvaux, T., Davis, K. J., Gaudet, B. J., Miles, N., Richardson, S. J., Wu, K., Sarmiento, D. P., Hardesty, R. M., and Bonin, T. A.: Toward reduced transport errors in a high resolution urban CO_2 inversion system, Elem Sci Anth, 5, 20, https://doi.org/10.1525/elementa.133, 2017.

Didan, K.: MOD13A3 MODIS/Terra Vegetation Indices Monthly L3 Global 1km SIN Grid V006, NASA Land Processes Distributed Active Archive Center [dataset], https://doi.org/10.5067/MODIS/MOD13A3.006, 2015.

Dusenge, M. E., Duarte, A. G., and Way, D. A.: Plant carbon metabolism and climate change: elevated CO_2 and temperature impacts on photosynthesis, photorespiration and respiration, New Phytol., 221, 32-49, https://doi.org/10.1111/nph.15283, 2019.

Fasoli, B.: uataq/stilt: Geoscientific Model Development 2018 (v1.0), Zenodo [code], https://doi.org/10.5281/zenodo.1196561, 2018.

Fasoli, B., Lin, J. C., Bowling, D. R., Mitchell, L., and Mendoza, D.: Simulating atmospheric tracer concentrations for spatially distributed receptors: updates to the Stochastic Time-Inverted Lagrangian Transport model's R interface (STILT-R version 2), Geosci. Model Dev., 11, 2813-2824, https://doi.org/10.5194/gmd-11-2813-2018, 2018.

Gao, S., Zhang, X., and Chen, M.: Spatiotemporal dynamics and driving forces of city-level CO_2 emissions in China from 2000 to 2019, J. Clean. Prod., 377, 134358, https://doi.org/10.1016/j.jclepro.2022.134358, 2022.

Gao, Y., Lee, X., Liu, S., Hu, N., Wei, X., Hu, C., Liu, C., Zhang, Z., and Yang, Y.: Spatiotemporal variability of the near-surface CO_2 concentration across an industrial-urban-rural transect, Nanjing, China, Sci. Total Environ., 631, 1192-1200, https://doi.org/10.1016/j.scitotenv.2018.03.126, 2018.

Gately, C. K. and Hutyra, L. R.: Large Uncertainties in Urban - Scale Carbon Emissions, J. Geophys. Res.-Atmos., 122, https://doi.org/10.1002/2017jd027359, 2017.

George, K., Ziska, L. H., Bunce, J. A., and Quebedeaux, B.: Elevated atmospheric CO_2 concentration and temperature across an urban–rural transect, Atmos. Environ., 41, 7654-7665, https://doi.org/10.1016/j.atmosenv.2007.08.018, 2007.

Gerbig, C., Lin, J., Wofsy, S., Daube, B., Andrews, A., Stephens, B., Bakwin, P., and Grainger, C.: Toward constraining regional - scale fluxes of CO_2 with atmospheric observations over a continent: 2. Analysis of COBRA data using a receptor - oriented framework, J. Geophys. Res.-Atmos., 108, https://doi.org/10.1029/2002JD003018, 2003.

Glauch, T., Marshall, J., Gerbig, C., Botía, S., Gałkowski, M., Vardag, S. N., and Butz, A.: pyVPRM: A next-generation Vegetation Photosynthesis and Respiration Model for the post-MODIS era, Geosci. Model Dev., 18, 4713-4742, https://doi.org/10.5194/gmd-18-4713-2025, 2025.

Griffin, R. J., Chen, J., Carmody, K., Vutukuru, S., and Dabdub, D.: Contribution of gas phase oxidation of volatile organic compounds to atmospheric carbon monoxide levels in two areas of the United States, J. Geophys. Res.-Atmos., 112, https://doi.org/10.1029/2006JD007602, 2007.

Guangzhou Municipal Bureau of Statistics: Guangzhou Statistical Yearbook 2024, Tech. rep., https://tjj.gz.gov.cn/datav/admin/home/www_nj/ (last access: 1 December 2025), 2024.

Gurney, K. R., Patarasuk, R., Liang, J., Song, Y., O'Keeffe, D., Rao, P., Whetstone, J. R., Duren, R. M., Eldering, A., and Miller, C.: The Hestia fossil fuel CO_2 emissions data product for the Los Angeles megacity (Hestia-LA), Earth Syst. Sci. Data, 11, 1309-1335, https://doi.org/10.5194/essd-11-1309-2019, 2019.

Han, P., Yao, B., Cai, Q., Chen, H., Sun, W., Liang, M., Zhang, X., Zhao, M., Martin, C., Liu, Z., Ye, H., Wang, P., Li, Y., and Zeng, N.: Support Carbon Neutral Goal with a High-Resolution Carbon Monitoring System in Beijing, B. Am. Meteorol. Soc., 105, E2461-E2481, https://doi.org/10.1175/bams-d-23-0025.1, 2024.

Han, S., Kondo, Y., Oshima, N., Takegawa, N., Miyazaki, Y., Hu, M., Lin, P., Deng, Z., Zhao, Y., and Sugimoto, N.: Temporal variations of elemental carbon in Beijing, J. Geophys. Res.-Atmos., 114, https://doi.org/10.1029/2009JD012027, 2009.

Hao, T., Chen, S., Liu, J., Tang, Y., and Han, S.: An observational study on the impact of sea-land breeze and low-level jet on air pollutant transport in the Bohai Bay, Atmos. Pollut. Res., 15, 102143, https://doi.org/10.1016/j.apr.2024.102143, 2024.

Hao, T., Chen, S., Cai, Z., Shan, X., Meng, L., Han, S., and Dong, G.: Influence of sea breeze on atmospheric pollutant concentration over Tianjin, China Environmental Science, 37(9), 3247-3257, https://doi.org/10.3969/j.issn.1000-6923.2017.09.006, 2017.

He, H., Kramer, R. J., Soden, B. J., and Jeevanjee, N.: State dependence of CO_2 forcing and its implications for climate sensitivity, Science, 382, 7, https://doi.org/10.1126/science.abq6872, 2023.

Hersbach, H., Bell, B., Berrisford, P., Biavati, G., Horányi, A., Muñoz Sabater, J., Nicolas, J., Peubey, C., Radu, R., Rozum, I., Schepers, D., Simmons, A., Soci, C., Dee, D., Thépaut, J-N: ERA5 hourly data on single levels from 1940 to present, Copernicus Climate Change Service (C3S) Climate Data Store (CDS) [dataset], https://doi.org/10.24381/cds.adbb2d47, 2023.

Hu, M., Wang, Y., Wang, S., Jiao, M., Huang, G., and Xia, B.: Spatial-temporal heterogeneity of air pollution and its relationship with meteorological factors in the Pearl River Delta, China, Atmos. Environ., 254, 118415, https://doi.org/10.1016/j.atmosenv.2021.118415, 2021.

Huang, Y., Li, S., Zhu, Y., Liu, Y., Hong, Y., Chen, X., Deng, W., Xi, X., Lu, X., and Fan, Q.: Increasing sea‐land breeze frequencies over coastal areas of China in the past five decades, Geophys. Res. Lett., 52, e2024GL112480, https://doi.org/10.1029/2024GL112480, 2025.

Hüser, I., Harder, H., Heil, A., and Kaiser, J. W.: Assumptions about footprint layer heights influence the quantification of emission sources: a case study for Cyprus, Atmos. Chem. Phys., 17, 10955-10967, https://doi.org/10.5194/acp-17-10955-2017, 2017.

Jacobson, A. R., Schuldt, K. N., Andrews, A., Miller, J. B., Oda, T., Basu, S., Mund, J., Weir, B., Ott, L., Aalto, T., Abshire, J. B., Aikin, K., Allen, G., Andrade, M., Apadula, F., Arnold, S., Baier, B., Bakwin, P., Bartyzel, J., Bentz, G., Bergamaschi, P., Beyersdorf, A., Biermann, T., Biraud, S. C., Blanc, P.-E., Boenisch, H., Bowling, D., Brailsford, G., Brand, W. A., Brunner, D., Bui, T. P., Burban, B., Bäni, L., Calzolari, F., Chang, C. S., Chen, H., Chen, G., Chmura, L., Clark, S., Climadat, S., Colomb, A., Commane, R., Condori, L., Conen, F., Conil, S., Couret, C., Cristofanelli, P., Cuevas, E., Curcoll, R., Daube, B., Davis, K. J., De Mazière, M., De Wekker, S., Dean-Day, J. M., Della Coletta, J., Delmotte, M., Di Iorio, T., DiGangi, E., DiGangi, J. P., Dickerson, R., Elsasser, M., Emmenegger, L., Fang, S., Forster, G., France, J., Frumau, A., Fuente-Lastra, M., Galkowski, M., Gatti, L. V., Gehrlein, T., Gerbig, C., Gheusi, F., Gloor, E., Goto, D., Griffis, T., Hammer, S., Hanisco, T. F., Hanson, C., Haszpra, L., Hatakka, J., Heimann, M., Heliasz, M., Heltai, D., Henne, S., Hensen, A., Hermans, C., Hermansen, O., Hintsa, E., Hoheisel, A., Holst, J., Iraci, L. T., Ivakhov, V., Jaffe, D. A., Jordan, A., Joubert, W., Kang, H.-Y., Karion, A., Kawa, S. R., Kazan, V., Keeling, R. F., Keronen, P., Kim, J., Klausen, J., Kneuer, T., Ko, M.-Y., Kolari, P., Kominkova, K., Kort, E., Kozlova, E., Krummel, P. B., Kubistin, D., Kulawik, S. S., Kumps, N., Labuschagne, C., Lam, D. H., Lan, X., Langenfelds, R. L., Lanza, A., Laurent, O., Laurila, T., Lauvaux, T., Lavric, J., Law, B. E., Lee, C.-H., Lee, J., Lehner, I., Lehtinen, K., Leppert, R., Leskinen, A., Leuenberger, M., Leung, W. H., Levin, I., Levula, J., Lin, J., Lindauer, M., Lindroth, A., Loh, Z. M., Lopez, M., Lunder, C. R., Löfvenius, M. O., Machida, T., Mammarella, I., Manca, G., Manning, A., Manning, A., Marek, M. V., Marklund, P., Marrero, J. E., Martin, M. Y., Martin, D., Martins, G. A., Matsueda, H.,

McKain, K., Meijer, H., Meinhardt, F., Merchant, L., Metzger, J.-M., Mihalopoulos, N., Miles, N. L., Miller, C. E., Mitchell, L., Monteiro, V., Montzka, S., Moossen, H., Moreno, C., Morgan, E., Morgui, J.-A., Morimoto, S., Munger, J. W., Munro, D., Mutuku, M., Myhre, C. L., Mölder, M., Müller-Williams, J., Nakaoka, S.-I., Necki, J., Newman, S., Nichol, S., Nisbet, E., Niwa, Y., Njiru, D. M., Noe, S. M., Nojiri, Y., O'Doherty, S., Obersteiner, F., Paplawsky, B., Parworth, C. L., Peischl, J., Peltola, O., Peters, W., Philippon, C., Piacentino, S., Pichon, J. M., Pickers, P., Piper, S., Pitt, J., Plass-Dülmer, C., Platt, S. M., Prinzivalli, S., Ramonet, M., Ramos, R., Ren, X., Reyes-Sanchez, E., Richardson, S. J., Rigouleau, L.-J., Riris, H., Rivas, P. P., Rothe, M., Roulet, Y.-A., Ryerson, T., Ryoo, J.-M., Sargent, M., Sasakawa, M., Schaefer, H., Scheeren, B., Schmidt, M., Schuck, T., Schumacher, M., Seibel, J., Seifert, T., Sha, M. K., Shepson, P., Shin, D., Shook, M., Sloop, C. D., Smale, D., Smith, P. D., Spain, G., St. Clair, J. M., Steger, D., Steinbacher, M., Stephens, B., Sweeney, C., Sørensen, L. L., Taipale, R., Takatsuji, S., Tans, P., Thoning, K., Timas, H., Torn, M., Trisolino, P., Turnbull, J., Vermeulen, A., Viner, B., Vitkova, G., Walker, S., Watson, A., Weiss, R., Weyrauch, D., Wofsy, S. C., Worsey, J., Worthy, D., Xueref-Remy, I., Yates, E. L., Young, D., Yver-Kwok, C., Zaehle, S., Zahn, A., Zellweger, C., Zimnoch, M., de Souza, R. A., di Sarra, A. G., van Dinther, D., and van den Bulk, P.: CarbonTracker CT-NRT.v2024-5, NOAA Earth System Research Laboratory [dataset], https://doi.org/10.15138/atpd-k925, 2024.

Kim, J., Berelson, W. M., Rollins, N. E., Asimow, N. G., Newman, C., Cohen, R. C., Miller, J. B., McDonald, B. C., Peischl, J., and Lehman, S. J.: Observing Anthropogenic and Biogenic CO_2 Emissions in Los Angeles Using a Dense Sensor Network, Environ Sci Technol, 59, 3508-3517, https://doi.org/10.1021/acs.est.4c11392, 2025.

Kumar, P.: Climate change and cities: challenges ahead, Front. Sustain. Cities, 3, 645613, https://doi.org/10.3389/frsc.2021.645613, 2021.

Kunik, L., Mallia, D. V., Gurney, K. R., Mendoza, D. L., Oda, T., and Lin, J. C.: Bayesian inverse estimation of urban CO_2 emissions: Results from a synthetic data simulation over Salt Lake City, UT, Elem Sci Anth, 7, 36, https://doi.org/10.1525/elementa.375, 2019.

Lauvaux, T., Miles, N. L., Deng, A., Richardson, S. J., Cambaliza, M. O., Davis, K. J., Gaudet, B., Gurney, K. R., Huang, J., O'Keefe, D., Song, Y., Karion, A., Oda, T., Patarasuk, R., Razlivanov, I., Sarmiento, D., Shepson, P., Sweeney, C., Turnbull, J., and Wu, K.: High-resolution atmospheric inversion of urban CO_2 emissions during the dormant season of the Indianapolis Flux Experiment (INFLUX), J. Geophys. Res.-Atmos., 121, 5213-5236, https://doi.org/10.1002/2015JD024473, 2016.

Lei, B.-Q., Li, L., and Chan, P. W.: Long-term trend in the sea-land breeze in Hong Kong, Urban. Clim., 55, 101981, https://doi.org/10.1016/j.uclim.2024.101981, 2024.

Leroyer, S., Bélair, S., Husain, S. Z., and Mailhot, J.: Subkilometer numerical weather prediction in an urban coastal area: A case study over the Vancouver metropolitan area, J. Appl. Meteorol. Clim., 53, 1433-1453, https://doi.org/10.1175/JAMC-D-13-0202.1, 2014.

Lian, J., Lauvaux, T., Utard, H., Bréon, F.-M., Broquet, G., Ramonet, M., Laurent, O., Albarus, I., Chariot, M., and Kotthaus, S.: Can we use atmospheric CO_2 measurements to verify emission trends reported by cities? Lessons from a 6-year atmospheric inversion over Paris, Atmos. Chem. Phys., 23, 8823-8835, https://doi.org/10.5194/acp-23-8823-2023, 2023.

Lin, J. C., Bares, R., Fasoli, B., Garcia, M., Crosman, E., and Lyman, S.: Declining methane emissions and steady, high leakage rates observed over multiple years in a western US oil/gas production basin, Sci. Rep-uk., 11, 22291, https://doi.org/10.1038/s41598-021-01721-5, 2021.

Lin, J. C., Gerbig, C., Wofsy, S., Andrews, A., Daube, B., Davis, K., and Grainger, C.: A near‐field tool for simulating the upstream influence of atmospheric observations: The Stochastic Time‐Inverted Lagrangian Transport (STILT) model, J. Geophys. Res.-Atmos., 108(D16), https://doi.org/10.1029/2002JD003161, 2003.

Liu, C., Huang, J.-P., Diao, Y.-W., Wen, X.-F., Xiao, W., Zhang, M., Lee, X.-H., and Liu, S.-D.: Optimization and evaluation of vegetation photosynthesis and respiration model using the measurements collected from the forest site of subtropical coniferous-evergreen, Chinese Journal of Plant Ecology, 39, 388-397, https://doi.org/10.17521/cjpe.2015.0038, 2015.

Liu, H., Chan, J. C., and Cheng, A. Y.: Internal boundary layer structure under sea-breeze conditions in Hong Kong, Atmos. Environ., 35, 683-692, https://doi.org/10.1016/S1352-2310(00)00335-6, 2001.

Liu, W., Niu, Z., Feng, X., Zhou, W., Liang, D., Wang, G., and Liu, L.: Determining the key meteorological factors affecting

atmospheric CO_2 and CH_4 using machine learning algorithms at a suburban site in China, Urban. Clim., 59, 102312, https://doi.org/10.1016/j.uclim.2025.102312, 2025.

Ma, M., Gao, Y., Ding, A., Su, H., Liao, H., Wang, S., Wang, X., Zhao, B., Zhang, S., Fu, P., Guenther, A. B., Wang, M., Li, S., Chu, B., Yao, X., and Gao, H.: Development and Assessment of a High-Resolution Biogenic Emission Inventory from Urban Green Spaces in China, Environ Sci Technol, 56, 175-184, https://doi.org/10.1021/acs.est.1c06170, 2022.

Mai, B., Deng, X., Liu, X., Li, T., Guo, J., and Ma, Q.: The climatology of ambient CO_2 concentrations from long-term observation in the Pearl River Delta region of China: Roles of anthropogenic and biogenic processes, Atmos. Environ., 251, 118266, https://doi.org/10.1016/j.atmosenv.2021.118266, 2021.

Mai, B., Diao, Y., Yang, H., Deng, T., Zou, Y., Wang, Y., Lan, W., Liu, X., and Deng, X.: Assessing atmospheric CO_2 concentrations and contributions from biogenic and anthropogenic sources in the Pearl River Delta region, Urban. Clim., 54, 101864, https://doi.org/10.1016/j.uclim.2024.101864, 2024a.

Mai, J., Yu, L., Deng, T., Wu, D., Qing, P., and Yu, X.: Impact of sea-land breezes on the ozone pollution over the Pearl River Estuary, China Environmental Science, 45(03), 1198-1209, https://doi.org/10.19674/j.cnki.issn1000-6923.20241102.001, 2024b.

Menzer, O. and McFadden, J. P.: Statistical partitioning of a three-year time series of direct urban net CO_2 flux measurements into biogenic and anthropogenic components, Atmos. Environ., 170, 319-333, https://doi.org/10.1016/j.atmosenv.2017.09.049, 2017.

Miller, J. B., Lehman, S. J., Verhulst, K. R., Miller, C. E., Duren, R. M., Yadav, V., Newman, S., and Sloop, C. D.: Large and seasonally varying biospheric CO_2 fluxes in the Los Angeles megacity revealed by atmospheric radiocarbon, P. Natl. Acad. Sci. Usa., 117, 26681-26687, https://doi.org/10.1073/pnas.2005253117, 2020.

Mitchell, L. E., Lin, J. C., Bowling, D. R., Pataki, D. E., Strong, C., Schauer, A. J., Bares, R., Bush, S. E., Stephens, B. B., and Mendoza, D.: Long-term urban carbon dioxide observations reveal spatial and temporal dynamics related to urban characteristics and growth, P. Natl. Acad. Sci. Usa., 115, 2912-2917, https://doi.org/10.1073/pnas.170239311, 2018.

Nalini, K., Lauvaux, T., Abdallah, C., Lian, J., Ciais, P., Utard, H., Laurent, O., and Ramonet, M.: High‐resolution Lagrangian inverse modeling of CO_2 emissions over the Paris region during the first 2020 lockdown period, J. Geophys. Res.-Atmos., 127, e2021JD036032, https://doi.org/10.1029/2021JD036032, 2022.

Newman, S., Jeong, S., Fischer, M., Xu, X., Haman, C., Lefer, B., Alvarez, S., Rappenglueck, B., Kort, E., and Andrews, A.: Diurnal tracking of anthropogenic CO_2 emissions in the Los Angeles basin megacity during spring 2010, Atmos. Chem. Phys., 13, 4359-4372, https://doi.org/10.5194/acp-13-4359-2013, 2013.

Pan, C., Zhu, X., Wei, N., Zhu, X., She, Q., Jia, W., Liu, M., and Xiang, W.: Spatial variability of daytime CO_2 concentration with landscape structure across urbanization gradients, Shanghai, China, Clim. Res., 69, 107-116, https://doi.org/10.3354/cr01394, 2016.

Park, C., Jeong, S., Shin, Y.-s., Cha, Y.-s., and Lee, H.-c.: Reduction in urban atmospheric CO_2 enhancement in Seoul, South Korea, resulting from social distancing policies during the COVID-19 pandemic, Atmos. Pollut. Res., 12, 101176, https://doi.org/10.1016/j.apr.2021.101176, 2021.

Pitt, J. R., Lopez-Coto, I., Hajny, K. D., Tomlin, J., Kaeser, R., Jayarathne, T., Stirm, B. H., Floerchinger, C. R., Loughner, C. P., and Gately, C. K.: New York City greenhouse gas emissions estimated with inverse modeling of aircraft measurements, Elem Sci Anth, 10, 00082, https://doi.org/10.1525/elementa.2021.00082, 2022.

Qingdao Municipal Bureau of Statistics: Qingdao Statistical Yearbook 2024, Tech. rep., http://qdtj.qingdao.gov.cn/tongjisj/tjsj_tjnj/tjnj_2024/202501/P020250114376271252952.pdf (last access: 1 December 2025), 2024.

Qiu, X. and Fan, S.: Study on the application of auto-meteorological station data in local circulations analysis such as the sea-land breeze, Acta Scientiarum Naturalium Universitatis Sunyatseni, 52(2), 133-136, https://doi.org/10.13471/j.cnki.acta.snus.2013.02.025, 2013.

Reddy, T. R., Mehta, S. K., Ananthavel, A., Ali, S., Annamalai, V., and Rao, D. N.: Seasonal characteristics of sea breeze and thermal internal boundary layer over Indian east coast region, Meteorol. Atmos. Phys., 133, 217-232,

https://doi.org/10.1007/s00703-020-00746-1, 2021.
Sargent, M., Barrera, Y., Nehrkorn, T., Hutyra, L. R., Gately, C. K., Jones, T., McKain, K., Sweeney, C., Hegarty, J., Hardiman, B., Wang, J. A., and Wofsy, S. C.: Anthropogenic and biogenic CO_2 fluxes in the Boston urban region, P. Natl. Acad. Sci. Usa., 115, 7491-7496, https://doi.org/10.1073/pnas.1803715115, 2018.
Schuldt, K. N., Mund, J., Aalto, T., Abshire, J. B., Aikin, K., Allen, G., Andrade, M., Andrews, A., Apadula, F., Arnold, S., Baier, B., Bakwin, P., Bartyzel, J., Bentz, G., Bergamaschi, P., Beyersdorf, A., Biermann, T., Biraud, S. C., Blanc, P.-E., Boenisch, H., Bowling, D., Brailsford, G., Brand, W. A., Brunner, D., Bui, T. P., Burban, B., Bäni, L., Calzolari, F., Chang, C. S., Chen, H., Chen, G., Chmura, L., Clark, S., Climadat, S., Colomb, A., Commane, R., Condori, L., Conen, F., Conil, S., Couret, C., Cristofanelli, P., Cuevas, E., Curcoll, R., Daube, B., Davis, K. J., De Mazière, M., De Wekker, S., Dean-Day, J. M., Della Coletta, J., Delmotte, M., Di Iorio, T., DiGangi, E., DiGangi, J. P., Dickerson, R., Elsasser, M., Emmenegger, L., Fang, S., Forster, G., France, J., Frumau, A., Fuente-Lastra, M., Galkowski, M., Gatti, L. V., Gehrlein, T., Gerbig, C., Gheusi, F., Gloor, E., Goto, D., Griffis, T., Hammer, S., Hanisco, T. F., Hanson, C., Haszpra, L., Hatakka, J., Heimann, M., Heliasz, M., Heltai, D., Henne, S., Hensen, A., Hermans, C., Hermansen, O., Hintsa, E., Hoheisel, A., Holst, J., Iraci, L. T., Ivakhov, V., Jaffe, D. A., Jordan, A., Joubert, W., Kang, H.-Y., Karion, A., Kawa, S. R., Kazan, V., Keeling, R. F., Keronen, P., Kim, J., Klausen, J., Kneuer, T., Ko, M.-Y., Kolari, P., Kominkova, K., Kort, E., Kozlova, E., Krummel, P. B., Kubistin, D., Kulawik, S. S., Kumps, N., Labuschagne, C., Lam, D. H., Lan, X., Langenfelds, R. L., Lanza, A., Laurent, O., Laurila, T., Lauvaux, T., Lavric, J., Law, B. E., Lee, C.-H., Lee, J., Lehner, I., Lehtinen, K., Leppert, R., Leskinen, A., Leuenberger, M., Leung, W. H., Levin, I., Levula, J., Lin, J., Lindauer, M., Lindroth, A., Loh, Z. M., Lopez, M., Lunder, C. R., Löfvenius, M. O., Machida, T., Mammarella, I., Manca, G., Manning, A., Manning, A., Marek, M. V., Marklund, P., Marrero, J. E., Martin, M. Y., Martin, D., Martins, G. A., Matsueda, H., McKain, K., Meijer, H., Meinhardt, F., Merchant, L., Metzger, J.-M., Mihalopoulos, N., Miles, N. L., Miller, C. E., Miller, J. B., Mitchell, L., Monteiro, V., Montzka, S., Moossen, H., Moreno, C., Morgan, E., Morgui, J.-A., Morimoto, S., Munger, J. W., Munro, D., Mutuku, M., Myhre, C. L., Mölder, M., Müller-Williams, J., Nakaoka, S.-I., Necki, J., Newman, S., Nichol, S., Nisbet, E., Niwa, Y., Njiru, D. M., Noe, S. M., Nojiri, Y., O'Doherty, S., Obersteiner, F., Paplawsky, B., Parworth, C. L., Peischl, J., Peltola, O., Peters, W., Philippon, C., Piacentino, S., Pichon, J. M., Pickers, P., Piper, S., Pitt, J., Plass-Dülmer, C., Platt, S. M., Prinzivalli, S., Ramonet, M., Ramos, R., Ren, X., Reyes-Sanchez, E., Richardson, S. J., Rigouleau, L.-J., Riris, H., Rivas, P. P., Rothe, M., Roulet, Y.-A., Ryerson, T., Ryoo, J.-M., Sargent, M., Sasakawa, M., Schaefer, H., Scheeren, B., Schmidt, M., Schuck, T., Schumacher, M., Seibel, J., Seifert, T., Sha, M. K., Shepson, P., Shin, D., Shook, M., Sloop, C. D., Smale, D., Smith, P. D., Spain, G., St. Clair, J. M., Steger, D., Steinbacher, M., Stephens, B., Sweeney, C., Sørensen, L. L., Taipale, R., Takatsuji, S., Tans, P., Thoning, K., Timas, H., Torn, M., Trisolino, P., Turnbull, J., Vermeulen, A., Viner, B., Vitkova, G., Walker, S., Watson, A., Weiss, R., Weyrauch, D., Wofsy, S. C., Worsey, J., Worthy, D., Xueref-Remy, I., Yates, E. L., Young, D., Yver-Kwok, C., Zaehle, S., Zahn, A., Zellweger, C., Zimnoch, M., de Souza, R. A., di Sarra, A. G., van Dinther, D., and van den Bulk, P.: Multi-laboratory compilation of atmospheric carbon dioxide data for the period 1957-2023 (obspack_co2_1_test_GLOBALVIEWplus_v10.1_2024-11-13), NOAA Earth System Research Laboratory, Global Monitoring Laboratory [dataset], https://doi.org/10.25925/20241101, 2024.
Shen, L., Zhao, C., and Yang, X.: Climate‐driven characteristics of sea‐land breezes over the globe, Geophys. Res. Lett., 48, e2020GL092308, https://doi.org/10.1029/2020GL092308, 2021.
Shen, L., Zhao, C., Ma, Z., Li, Z., Li, J., and Wang, K.: Observed decrease of summer sea-land breeze in Shanghai from 1994 to 2014 and its association with urbanization, Atmos. Res., 227, 198-209, https://doi.org/10.1016/j.atmosres.2019.05.007, 2019.
Shen, L., Zhao, C., Xu, C., Yan, Y., Chen, A., Yang, Y., Hang, R., Zhu, Y., Zhang, Z., and Song, X.: Effects of sea land breeze on air‐sea turbulent heat fluxes in different seasons using platform observation in East China Sea, J. Geophys. Res.-Atmos., 129, e2023JD040001, https://doi.org/10.1029/2023JD040001, 2024.
Shenzhen Municipal Bureau of Statistics: Shenzhen Statistical Yearbook, Tech. rep., https://tjj.sz.gov.cn/attachment/1/1568/1568796/12061198.pdf (last access: 1 December 2025), 2024.
Shusterman, A. A., Kim, J., Lieschke, K. J., Newman, C., Wooldridge, P. J., and Cohen, R. C.: Observing local CO_2 sources

using low-cost, near-surface urban monitors, Atmos. Chem. Phys., 18, 13773-13785, https://doi.org/10.5194/acp-18-13773-2018, 2018.

Soininen, J., Kohonen, K.-M., Rantala, P., Kulmala, L., Aaltonen, H., and Järvi, L.: Carbon uptake of an urban green space inferred from carbonyl sulfide fluxes, npj Clim Atmos Sci, 8, https://doi.org/10.1038/s41612-025-00958-5, 2025.

Stauffer, R. M., Thompson, A. M., Martins, D. K., Clark, R. D., Goldberg, D. L., Loughner, C. P., Delgado, R., Dickerson, R. R., Stehr, J. W., and Tzortziou, M. A.: Bay breeze influence on surface ozone at Edgewood, MD during July 2011, J. Atmos. Chem., 72, 335-353, https://doi.org/10.1007/s10874-012-9241-6, 2015.

Sun, L., Tian, W., Zhang, W., Liu, C., and Fang, C.: Characteristics of sea-land breezes and their impact on $PM_{2.5}$ and O_3 in Shanghai and adjacent areas, Acta Scientiae Circumstantiae, 42(9), 339-350, https://doi.org/10.13671/j.hjkxxb.2022.0111, 2022.

Tianjin Municipal Bureau of Statistics: Tianjin Statistical Yearbook, Tech. rep., https://stats.tj.gov.cn/nianjian/2024nj/zk/indexch.htm (last access: 1 December 2025), 2024.

Turnbull, J. C., Karion, A., Davis, K. J., Lauvaux, T., Miles, N. L., Richardson, S. J., Sweeney, C., McKain, K., Lehman, S. J., and Gurney, K. R.: Synthesis of urban CO_2 emission estimates from multiple methods from the Indianapolis Flux Project (INFLUX), Environ. Sci. Technol., 53, 287-295, https://doi.org/10.1021/acs.est.8b05552, 2018.

Turnbull, J. C., Sweeney, C., Karion, A., Newberger, T., Lehman, S. J., Tans, P. P., Davis, K. J., Lauvaux, T., Miles, N. L., and Richardson, S. J.: Toward quantification and source sector identification of fossil fuel CO_2 emissions from an urban area: Results from the INFLUX experiment, J. Geophys. Res.-Atmos., 120, 292-312, https://doi.org/10.1002/2014JD022555, 2015.

Turnbull, J. C., Tans, P. P., Lehman, S. J., Baker, D., Conway, T. J., Chung, Y., Gregg, J., Miller, J. B., Southon, J. R., and Zhou, L. X.: Atmospheric observations of carbon monoxide and fossil fuel CO_2 emissions from East Asia, J. Geophys. Res.-Atmos., 116, https://doi.org/10.1029/2011JD016691, 2011.

Velasco, E., Roth, M., Tan, S., Quak, M., Nabarro, S., and Norford, L.: The role of vegetation in the CO_2 flux from a tropical urban neighbourhood, Atmos. Chem. Phys., 13, 10185-10202, https://doi.org/10.5194/acp-13-10185-2013, 2013.

Verhulst, K. R., Karion, A., Kim, J., Salameh, P. K., Keeling, R. F., Newman, S., Miller, J., Sloop, C., Pongetti, T., and Rao, P.: Carbon dioxide and methane measurements from the Los Angeles Megacity Carbon Project–Part 1: calibration, urban enhancements, and uncertainty estimates, Atmos. Chem. Phys., 17, 8313-8341, https://doi.org/10.5194/acp-17-8313-2017, 2017.

Vimont, I. J., Turnbull, J. C., Petrenko, V. V., Place, P. F., Sweeney, C., Miles, N., Richardson, S., Vaughn, B. H., and White, J. W.: An improved estimate for the $\delta^{13}C$ and $\delta^{18}O$ signatures of carbon monoxide produced from atmospheric oxidation of volatile organic compounds, Atmos. Chem. Phys., 19, 8547-8562, https://doi.org/10.5194/acp-19-8547-2019, 2019.

Wang, B., Geddes, J. A., Adams, T. J., Lind, E. S., McDonald, B. C., He, J., Harkins, C., Li, D., and Pfister, G. G.: Implications of sea breezes on air quality monitoring in a coastal urban environment: Evidence from high resolution modeling of NO_2 and O_3, J. Geophys. Res.-Atmos., 128, e2022JD037860, https://doi.org/10.1029/2022JD037860, 2023.

Wang, P., Zhou, W., Niu, Z., Xiong, X., Wu, S., Cheng, P., Hou, Y., Lu, X., and Du, H.: Spatio-temporal variability of atmospheric CO_2 and its main causes: A case study in Xi'an city, China, Atmos. Res., 249, 105346, https://doi.org/10.1016/j.atmosres.2020.105346, 2021.

Wang, P., Zhou, W., Xiong, X., Wu, S., Niu, Z., Yu, Y., Liu, J., Feng, T., Cheng, P., and Du, H.: Source attribution of atmospheric CO_2 using ^{14}C and ^{13}C as tracers in two Chinese megacities during winter, J. Geophys. Res.-Atmos., 127, e2022JD036504, https://doi.org/10.1029/2022JD036504, 2022.

Wang, Y., Munger, J., Xu, S., McElroy, M. B., Hao, J., Nielsen, C., and Ma, H.: CO_2 and its correlation with CO at a rural site near Beijing: implications for combustion efficiency in China, Atmos. Chem. Phys., 10, 8881-8897, https://doi.org/10.5194/acp-10-8881-2010, 2010.

Wei, D., Reinmann, A., Schiferl, L. D., and Commane, R.: High resolution modeling of vegetation reveals large summertime biogenic CO_2 fluxes in New York City, Environ. Res. Lett., 17, 124031, https://doi.org/10.1088/1748-9326/aca68f, 2022.

WMO: WMO Greenhouse Gas Bulletin No. 20 – The State of Greenhouse Gases in the Atmosphere Based on Global

Observations through 2023, Tech. rep., https://library.wmo.int/idurl/4/69057 (last access: 18 June 2025), 2024.
WMO: GAW Report No. 314 – Integrated Global Greenhouse Gas Information System: Urban Emission Observation and Monitoring Good Research Practice Guidelines, Tech. rep., https://library.wmo.int/idurl/4/69623 (last access: 1 December 2025), 2025.
Wu, D., Lin, J. C., Duarte, H. F., Yadav, V., Parazoo, N. C., Oda, T., and Kort, E. A.: A model for urban biogenic CO_2 fluxes: Solar-Induced Fluorescence for Modeling Urban biogenic Fluxes (SMUrF v1), Geosci. Model Dev., 14, 3633-3661, https://doi.org/10.5194/gmd-14-3633-2021, 2021.
Wu, D., Liu, J., Wennberg, P. O., Palmer, P. I., Nelson, R. R., Kiel, M., and Eldering, A.: Towards sector-based attribution using intra-city variations in satellite-based emission ratios between CO_2 and CO, Atmos. Chem. Phys., 22, 14547-14570, https://doi.org/10.5194/acp-22-14547-2022, 2022a.
Wu, K., Davis, K. J., Miles, N. L., Richardson, S. J., Lauvaux, T., Sarmiento, D. P., Balashov, N. V., Keller, K., Turnbull, J., and Gurney, K. R.: Source decomposition of eddy-covariance CO_2 flux measurements for evaluating a high-resolution urban CO_2 emissions inventory, Environ. Res. Lett., 17, 074035, https://doi.org/10.1088/1748-9326/ac7c29, 2022b.
Wu, M., Wu, D., Fan, Q., Wang, B. M., Li, H. W., and Fan, S. J.: Observational studies of the meteorological characteristics associated with poor air quality over the Pearl River Delta in China, Atmos. Chem. Phys., 13, 10755-10766, https://doi.org/10.5194/acp-13-10755-2013, 2013.
Xu, R., Tong, D., Xiao, Q., Qin, X., Chen, C., Yan, L., Cheng, J., Cui, C., Hu, H., and Liu, W.: MEIC-global-CO_2: A new global CO_2 emission inventory with highly-resolved source category and sub-country information, Sci. China Earth Sci, 67, 450-465, https://doi.org/10.1007/s11430-023-1230-3, 2024.
Xueref-Remy, I., Dieudonné, E., Vuillemin, C., Lopez, M., Lac, C., Schmidt, M., Delmotte, M., Chevallier, F., Ravetta, F., Perrussel, O., Ciais, P., Bréon, F.-M., Broquet, G., Ramonet, M., Spain, T. G., and Ampe, C.: Diurnal, synoptic and seasonal variability of atmospheric CO_2 in the Paris megacity area, Atmos. Chem. Phys., 18, 3335-3362, https://doi.org/10.5194/acp-18-3335-2018, 2018.
Yadav, V., Ghosh, S., Mueller, K., Karion, A., Roest, G., Gourdji, S. M., Lopez‐Coto, I., Gurney, K. R., Parazoo, N., and Verhulst, K. R.: The impact of COVID‐19 on CO_2 emissions in the Los Angeles and Washington DC/Baltimore metropolitan areas, Geophys. Res. Lett., 48, e2021GL092744, https://doi.org/10.1029/2021GL092744, 2021.
Yang, H., Wu, K., Shen, H., Janssens-Maenhout, G., Crippa, M., Guizzardi, D., and Zhou, M.: A comparative analysis of China's anthropogenic CO_2 emissions (2000–2023): insights from six bottom-up inventories and uncertainty assessment, Atmos. Chem. Phys., 25, 18111-18127, https://doi.org/10.5194/acp-25-18111-2025, 2025.
Yang, J. and Huang, X.: The 30 m annual land cover datasets and its dynamics in China from 1985 to 2024, Earth System Science Data [dataset], https://doi.org/10.5281/zenodo.15853565, 2025.
Yang, T., Li, H. Y., Cao, J., Lu, Q. Q., Wang, Z. F., He, L. T., Sun, H. H., and Han, K.: Investigating the climatology of North China's urban inland lake based on six years of observations, Sci. Total Environ., 826, https://doi.org/10.1016/j.scitotenv.2022.154120, 2022.
Yang, Y., Zhou, M., Wang, T., Yao, B., Han, P., Ji, D., Zhou, W., Sun, Y., Wang, G., and Wang, P.: Spatial and temporal variations of CO_2 mole fractions observed at Beijing, Xianghe, and Xinglong in North China, Atmos. Chem. Phys., 21, 11741-11757, https://doi.org/10.5194/acp-21-11741-2021, 2021.
Ye, X., Lauvaux, T., Kort, E. A., Oda, T., Feng, S., Lin, J. C., Yang, E. G., and Wu, D.: Constraining fossil fuel CO_2 emissions from urban area using OCO‐2 observations of total column CO_2, J. Geophys. Res.-Atmos., 125, e2019JD030528, https://doi.org/10.1029/2019JD030528, 2020.
You, C. and Chi-Hung Fung, J.: Characteristics of the Sea-Breeze Circulation in the Pearl River Delta Region and Its Dynamical Diagnosis, J. Appl. Meteorol. Clim., 58, 741-755, https://doi.org/10.1175/jamc-d-18-0153.1, 2019.
Young, H. A., Turnbull, J. C., Keller, E. D., Domingues, L. G., Parry-Thompson, J., Hilton, T. W., Brailsford, G. W., Gray, S., Moss, R. C., and Mikaloff-Fletcher, S.: Urban flask measurements of CO_2ff and CO to identify emission sources at different site types in Auckland, New Zealand, Philosophical Transactions of the Royal Society A, 381, 20220204, https://doi.org/10.1098/rsta.2022.0204, 2023.

Zhang, L., Lin, J., Shao, Y., Huang, S., Fan, S., and Wei, W.: Understanding the impact of sea and land breezes on ozone pollution in the Pearl River Delta, Acta Scientiae Circumstantiae, 44(1), 74-85, https://doi.org/10.13671/j.hjkxxb.2023.0285, 2024.

Zhao, D., Xin, J., Wang, W., Jia, D., Wang, Z., Xiao, H., Liu, C., Zhou, J., Tong, L., and Ma, Y.: Effects of the sea-land breeze on coastal ozone pollution in the Yangtze River Delta, China, Sci. Total Environ., 807, 150306, https://doi.org/10.1016/j.scitotenv.2021.150306, 2022.

Zheng, B., Tong, D., Li, M., Liu, F., Hong, C., Geng, G., Li, H., Li, X., Peng, L., Qi, J., Yan, L., Zhang, Y., Zhao, H., Zheng, Y., He, K., and Zhang, Q.: Trends in China's anthropogenic emissions since 2010 as the consequence of clean air actions, Atmos. Chem. Phys., 18, 14095-14111, https://doi.org/10.5194/acp-18-14095-2018, 2018.

Zheng, Y., Jiang, F., Feng, S., Shen, Y., Liu, H., Guo, H., Lyu, X., Jia, M., and Lou, C.: Large-scale land-sea interactions extend ozone pollution duration in coastal cities along northern China, Env. Sci. Ecotechnol., 18, 100322, https://doi.org/10.1016/j.ese.2023.100322, 2024.